The Magazine for Nanoscience and Technology
VOL 27 FALL 2024

NANOscientific

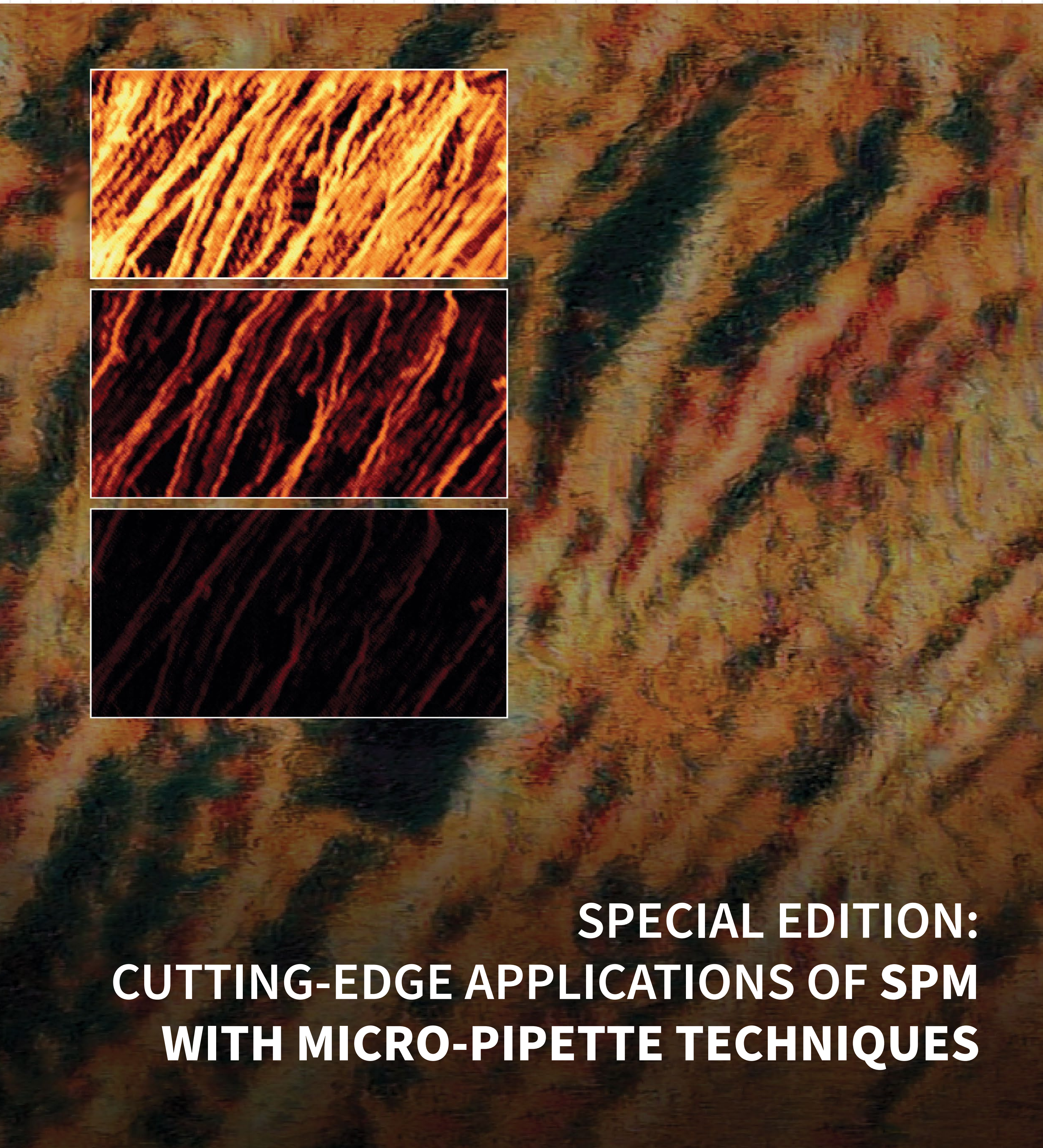

SPECIAL EDITION: CUTTING-EDGE APPLICATIONS OF SPM WITH MICRO-PIPETTE TECHNIQUES

MAPPING ELECTROACTIVITY OF HOPG: INSIGHTS INTO ELECTROCATALYSIS WITH SECCM

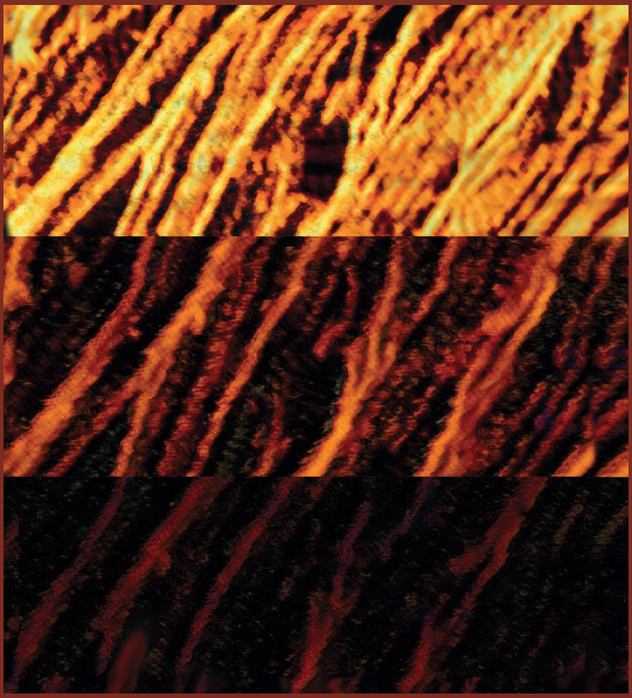

Sample: Highly Oriented Pyrolytic Graphite (HOPG)
Mode: SECCM
Instrument: Park NX12 configured with a dual-barrel SECCM system

The front cover features SECCM electroactivity maps of HOPG, measured at different potentials (-0.25 V, -0.30 V, and -0.50 V vs Ag/AgCl) on the same area. The probe, with a diameter of approximately 200 nm, was modulated by 10 nm to operate in AC mode SECCM, using 5 mM $Ru(NH_3)_6Cl_3$ and 25 mM KCl as the reference electrolyte.

HOPG serves as an ideal model electrode for developing and optimizing electrocatalytic materials and reactions essential for energy conversion. Analyzing its electrochemical behavior provides valuable insights into electrocatalysis mechanisms, guiding the design of more efficient catalysts for various applications.

INDEX

NANO scientific

- **Keibock Lee**, Editor-in-Chief
  keibock@nanoscientific.org
- **Jessica Kang**, Managing Editor
- **Sun Ham**, Editor and Point of Contact
  sun.ham@parksystems.com
- **Cathy Lee,** Technical Editor
- **Ester Cho**, Art Director

Publisher and Corporate officers
- **Sang-il Park**, Chief Executive Officer
- **Karen Cho,** EVP of Operations Management Division
- **Ryan Yoo,** EVP of Business Development
- **Sang-Joon Cho**, EVP of Research Equipment Business Unit
- **Richard Lee**, EVP of Industrial Equipment Business Unit

NanoScientific is published both in print and online to showcase advancements in the field of nanoscience and technology across a wide range of multidisciplinary areas of research. The publication is offered free to anyone who works or have interest in the field of nanotechnology, nanoscience, microscopy and other related fields of study and manufacturing.

We enjoy hearing from you, our readers.
Please send your research or story ideas to sun.ham@parksystems.com.
To view all of our articles, please visit our web site at nanoscientific.org.

HIGH-RESOLUTION MEASUREMENT OF POTENTIAL-DEPENDENT ELECTROCHEMICAL ACTIVITIES ON HOPG USING SCANNING ELECTROCHEMICAL CELL MICROSCOPY (SECCM)

Myung-Hoon Choi,[1] Hanaul Noh, [1] Lane A. Baker[2] and Stefan B Kaemmer[1]
Park Systems Inc., Santa Clara, CA USA. Department of Chemistry, Texas A&M University, College Station, TX, USA

ABSTRACT

Scanning Electrochemical Cell Microscopy (SECCM) offers enhanced spatial resolution for visualizing electroactivity on surfaces. This study reveals potential-dependent electroactivity trends at both step edges and the basal plane of HOPG from the concurrent acquisition of topographical information and corresponding faradaic current maps. Statistical analysis of step edges underscores the relationship between thickness and electroactivity, contributing insights into the heterogeneous electroactivity patterns. The applied methodology allows for simultaneous topography and electroactivity mapping, with minimal electrolyte spread during potential-based measurements. These findings advance our understanding of electrocatalysis and its relevance for catalyst design and energy conversion processes with high accuracy and reliability.

Introduction

Highly Oriented Pyrolytic Graphite (HOPG) is a popular substrate for Scanning Probe Microscopy (SPM) research due to its flatness, uniformity, and ordered layered structure. HOPG has been extensively used as a model electrode for developing and optimizing electrocatalytic materials and reactions crucial in energy conversion processes [1-4]. By studying electrochemical behavior, one can gain insights into the fundamental mechanisms of electrocatalysis, enabling the design of more efficient catalysts for a variety of applications. From a microscopic viewpoint, the basal plane and edge of the HOPG surface exhibit heterogeneous electro- and electrocatalytic characteristics due to differences in their electronic and structural properties [5]. Conventionally, Scanning Electrochemical Microscopy (SECM) is employed to study the electrochemical heterogeneity at surfaces allowing for the visualization of electrochemical processes [6]. By using a microelectrode probe, SECM measures the electrochemical activity of local areas, providing information on electrocatalytic properties. In comparison, SECCM offers higher spatial resolution measurements than SECM, thus providing more spatially localized information about the electrochemical activity. SECCM works by using a small meniscus formed at the pipette tip end as a probe and electrochemical cell, allowing for precise delivery of reactants to a specific location on the surface [7-10].

This study demonstrates the visualization of the heterogeneity in the electrochemical activities of HOPG using a customized Park Systems SECCM setup that allows for the simultaneous acquisition of topography and electrochemical activity maps. The grade 2 HOPG used in this study possesses an intermediate quality, making it suitable for both extensive use and high-resolution imaging purposes. A series of electrochemical maps at different potentials applied to the HOPG substrate were acquired by operating SECCM in AC-mode, which was previously demonstrated [11, 12].

Experimental

Chemical and Materials

All solutions were prepared at 25 °C using ultrapure H_2O obtained from a Milli-Q water purification system (with a resistivity of 18.2 MΩ·cm, Millipore Corp.). The chemicals used, including potassium chloride (KCl, VWR Analytical), were used as received. HOPG grade 2 (SPI) was utilized as the substrate in the experiments. The ruthenium hexamine redox couple was purchased from Sigma-Aldrich and stored at room temperature before utilization.

Dual Barrel Probe Fabrication and Use

Theta borosilicate capillaries (O.D. 1.2 mm, I.D. 0.9 mm) were transformed into nanopipettes (I.D. 50-70 nm, O.D. 150-200 nm) using a CO_2 laser puller (P-2000, Sutter Instruments). The pipette dimensions were confirmed with SEM (FEI Quanta 600F). The pipettes were loaded with specific solutions, such as 100 mM KCl and 5 mM $Ru(NH_3)_6Cl_3$. Two Ag/AgCl wires were inserted into each barrel of the pipette, serving as quasi-reference counter electrodes (QRCEs).

SECCM Instrumentation

The SECCM system with a dual-barrel configuration was developed on a Park NX12 AFM platform (Park Systems) [11, 12], integrating a custom-built potentiostat. The current readings obtained from the potentiostat were fed into the Aux channel of the AFM controller. These current readings were crucial in maintaining a consistent distance between the probe tip and the HOPG sample surface throughout the SECCM measurements. For stable SECCM cyclic voltammetry (CV) mapping operations and measurements, a custom-built humidity chamber was employed to maintain humidity levels between 20%-40%. The SECCM measurment was carried out in collaboration with the Baker Lab at Department of Chemistry in Texas A&M University.

Results and Discussion

The operational principles of the SECCM instrumentation have been thoroughly described in prior publications by the Unwin group [7-10]. The key element is a symmetrically fabricated dual-barrel probe. This importance stems from the fact that within an SECCM setup, the electrolyte meniscus functions as a miniature electrochemical cell. The size of this meniscus typically falls within the attoliter range, and its dimensions are intricately linked to those of the probe tip, which usually measures between 150-250 nanometers in outer diameter

(Fig. 1). The vertical view revealed the true shape of the dual-barrel probe in an ecliptic structure (Fig. 1A and 1B). The dual-barrel probes that were pulled demonstrated a linear ohmic response between the two barrels used in SECCM measurements (Fig. 1C).

To ensure safe and consistent contact of the meniscus with the substrate, which serves as the working electrode, we meticulously monitored the ionic current in both DC and AC components. Once the meniscus contacted the substrate, we initiated a potential sweep (V_1) ranging from 0 to -0.5 V to acquire cyclic voltammograms. Using the potentiostat, the desired potential difference was achieved by applying ± $V_{1/2}$ to two Ag/AgCl electrodes. As a result, the effective potential (Vwe) at the substrate, relative to the Ag/AgCl electrodes, was approximately -V_1. The electrochemical current signal (mi_{we}) generated at the working electrode was accurately recorded (Fig. 2A) using a built-in current amplifier of the AFM. We compared two CVs obtained at different scan rates, 10 and 50 mV/s, using the $Ru(NH_3)_6^{2+}$ /$Ru(NH_3)_6^{3+}$ redox couple through nanoscale cyclic voltammetry, facilitated by the dual barrel SECCM setup. The CVs exhibited a typical steady-state current pattern characteristic of ultramicroelectrodes, and notably, they appeared nearly identical, suggesting that the electrochemical response remains consistent regardless of the scan rate (Fig. 2B).

Simultaneous and correlative SECCM topography and electroactivity images of HOPG during reversible electron transfer measurements with ruthenium hexamine were successfully obtained (Fig. 3). The lateral image resolution obtained was equivalent to the diameter of the dual barrel probe tip. This suggests that the electrolyte meniscus did not spread out to the substrate surface during the measurement when the applied potential was present. To investigate the potential-dependent electroactivity, measurements were conducted at working electrode potentials of - 0.25, - 0.3, and - 0.5 V vs Ag/AgCl. The results revealed that higher applied potentials corresponded to higher electroactivity at both the step edges and the basal plane. Specifically, at the step edge, the electroactivity ranged from 8 to 22 pA (max.), while at the basal plane, it ranged from 5 pA to 15 pA (max.) from the line profile analysis (Fig. 4). SECCM enabled correlative data analysis of the characterization of position (or thickness)-dependent electroactivity.

The in-depth analysis included comparing line profiles of thickness and faradaic current at 7 distinct step edges (Fig. 4). This approach allowed us to characterize the heterogeneous electroactivity, expressed as the faradaic current per single layer of graphene. The estimated number of single graphene layers ranged

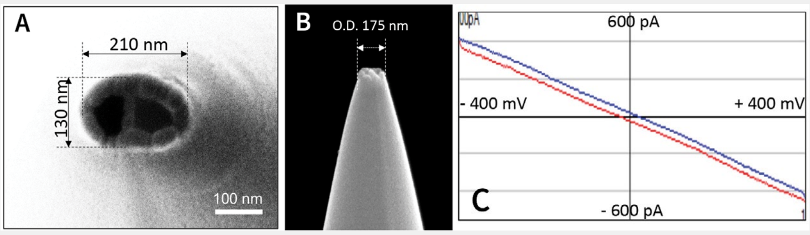

Fig. 1. SEM images of the dual barrel probe, a vertical view (A), and a side view (B), which shows the approximate diameter of the probe-tip as 200 nm. The corresponding ohmic response of the dual barrel probe (C) was measured after filling it with 100 mM KCl and applying a potential range of -0.4 V to + 0.4 V. The resulting resistance was determined to be approximately 1 GΩ.

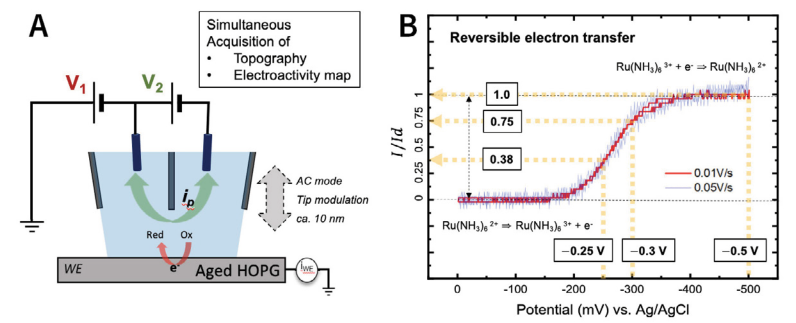

Fig. 2. Dual barrel SECCM diagram of the system configuration (A) and SECCM cyclic voltammograms (B) with 5 mM $Ru(NH_3)_6Cl_3$ (redox couple), 25 mM KCl (reference electrolyte), substrate (WE): HOPG, probe tip diameter: ~ 200 nm, ionic current 24 pA / 100 mV (V_2)

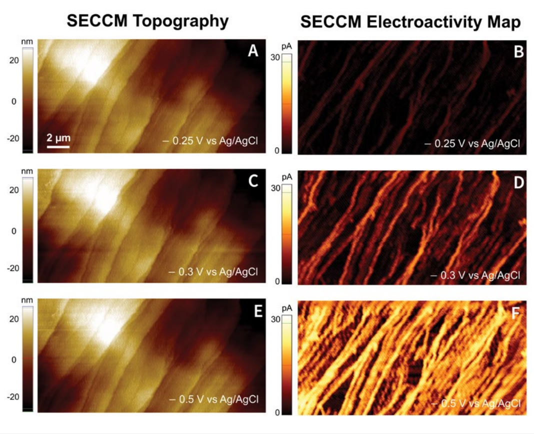

Fig. 3. SECCM Topographies (A,C,E) and SECCM electroactivity maps (B,D,F) of HOPG. The reduction of $Ru(NH_3)_6^{3+}$ of the same area was measured by applying different potentials of - 0.25 V (B), - 0.30 V (D), and - 0.50 V (F) vs Ag/AgCl. The probe diameter was ca. 200 nm and the probe was modulated by 10 nm to operate in AC mode SECCM. 5 mM $Ru(NH_3)_6Cl_3$ was filled into both barrels of the probe with 25 mM KCl as reference electrolyte.

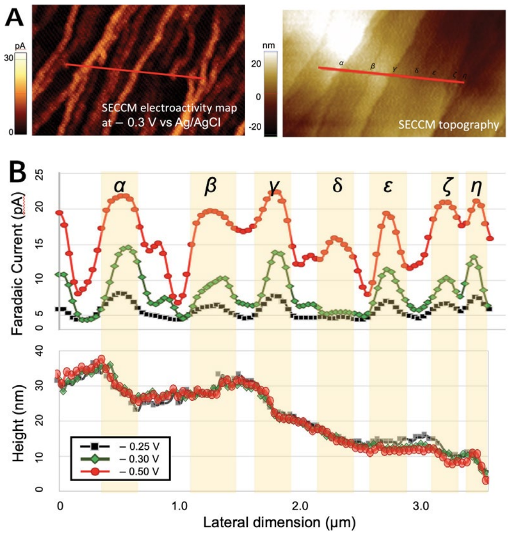

Fig. 4. Selected linear area of SECCM electroactivity map (top) and topography (bottom) of HOPG for line profile comparison (A). The line profiles of both were extracted from the red lines above from each at three different potentials of - 0.25 V, - 0.3 V, and - 0.5 V vs Ag/AgCl. (B) correlative profile comparison of selected line data extracted from electroactivity map and corresponding topography at three different potential levels. A total of seven step-edges(α-η) were chosen along the selected line (the red bar in (A)).

from 6 to 30. By directly comparing topography with faradaic current, we were able to assess the variation in electroactivity at individual step edges on the HOPG surface. Additionally, we observed clear potential-dependent effects in each local area (Fig. 4B).

At last, the electroactivity of step edges on HOPG was selectively investigated using statistical analysis. The analysis focused on step edges with a thickness ranging from 8 nm to 20 nm. The dataset consisted of 1727, 1902, and 1870 data points for the electroactivity map at potentials of - 0.25 V, - 0.3 V, and - 0.5 V, respectively (Fig. 5A). A box-and-whisker analysis revealed a clear trend: as the step edges became thicker, the electroactivity increased, and the variation in electroactivity decreased. This trend was observed consistently across all three potentials (Fig. 5B and Table 1).

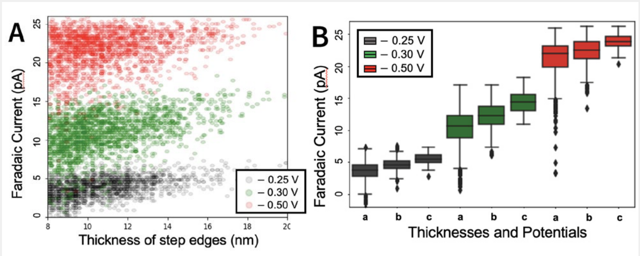

Fig. 5. Statistical distribution of the faradaic current at step edges in the range of 8 to 20 nm for three different potentials: - 0.25 V, - 0.3 V, and - 0.5 V vs Ag/AgCl. (A) individual data plots, (B) Box-and-whisker plot depicting the statistical relationship between the thickness of step edges (A: 8-12 nm, B: 12-16 nm, C: 16-20 nm) and three different potentials: - 0.25 V (gray), - 0.3 V (green), and - 0.5 V (red) vs Ag/AgCl. The data are presented in Table 1.

Table 1. Statistical analysis of the calculated electroactivity in different thickness levels and potential range.

	a:8-12 nm	b:12-16 nm	c:16-20 nm	Ave (stdev.)
E_{we} −0.25 V	3.5 (±1.4)	4.1 (±1.1)	5.6 (±1.0)	3.8 (±1.4)
E_{we} −0.3 V	10.4(±2.0)	12.3(±2.0)	14.5 (±1.6)	10.9 (±2.6)
E_{we} −0.5 V	21.3 (±2.8)	22.4 (±2.0)	24.1 (±1.2)	21.7 (±2.6)

Conclusions

In conclusion, the dual barrel SECCM system has proven to be a valuable tool for electrochemistry researchers by employing a custom-designed potentiostat. It allows for simultaneous high-resolution topography and electroactivity imaging while effectively containing the electrolyte during measurements with applied potential. On the model system used, our study revealed a clear relationship between higher applied potentials and increased electroactivity at both step edges and the basal plane of HOPG. Additionally, our analysis of thickness-dependent electroactivity offered valuable information, estimating the number of single graphene layers. We have demonstrated that dual barrel SECCM is a useful tool for electrochemistry researchers, facilitating a deeper understanding of electrocatalysis and its potential applications in catalyst development and energy conversion processes.

References

1. Banerjee, S.; Sardar, M.; Gayathri, N.; Tyagi, A.K.; and Raj, B., Phys. Rev. B, 2005, 72, 075418.
2. Ma, H.; Lee, L.; Brooksby, P.A.; Brown, S.A.; Fraser, S.J.; Gordon, K.C.; Leroux, Y.R.; Hapiot, P.; Downard, A. J., J. Phys. Chem. C, 2014, 118 (11), 5820-5826.
3. Pham, K. D.; Hieu, N.N.; Phuc, H.V.; Fedorov, I.A.; Duque, C.A.; Amin, B.; Nguyen, C.V., Appl. Phys. Lett. 2018, 113, 171605.
4. Tao, L.; Qiao,M.; Jin, R.; Li, Y.; Xiao, Z.; Wang, Y.; Zhang, N.; Xie, C.; He, Q.; Jiang, D.; Yu, G.; Li, Y.; Wang, Sh., Angew. Chem. Int. Ed. 2019, 58, 1-7.
5. Jaouen, K.; Henrotte, O.; Campidelli, S.; Jousselme, B.; Derycke, V.; Cornut, R., Appl. Mater. Today, 2017, 8, 116-124.
6. Nioradze, N.; Chen, R.; Kurapati, N.; Khvataeva-Domanov, A.; Mabic, S.; Amemiya, S., Anal. Chem., 2015, 87 (9), 4836-4843.
7. Snowden, M.E.; Güell, A.G.; Lai, S. C. S.; McKelvey, K.; Ebejer, N.; O'Connell, M.A.; Colburn, A.W.; Unwin, P.R.,Anal. Chem., 2012, 84 (5), 2483-2491.
8. Patel, A.N.; Collignon, M.G.; O'Connell, M.A.; Hung, W.O.Y.; McKelvey, K.; Macpherson, J.V.; Unwin, P.R., J. Am. Chem. Soc., 2012, 134 (49), 20117-20130.
9. Lai, S.C.S., Patel, A.N., McKelvey, K. and Unwin, P.R., Angew. Chem. Int. Ed., 2012, 51, 5405-5408.
10. Zhang, J. and Kim, B. Park AFM Application Note #48
11. Choi, M.-H.; Siepser, N.P.; Jeong, S.-J.; Wang, Y.; Jagdale, G.; Ye, X.; and Baker, L. A., Nano Lett. 2020, 20 (2), 1233-1239.
12. Jeong, S.‡; Choi, M.-H.‡; Jagdale, G.; Zhong Y.; Siepser, N.P.; Wang, Y.; Baker, L.A.; Ye, X. J. Am. Chem. Soc. 2022, 144, 28, 12673–12680

NANOSCIENTIFIC MAGAZINE INTERVIEW

Professor Michael V. Mirkin
Dept. of Chemistry, Queens College, NY, USA

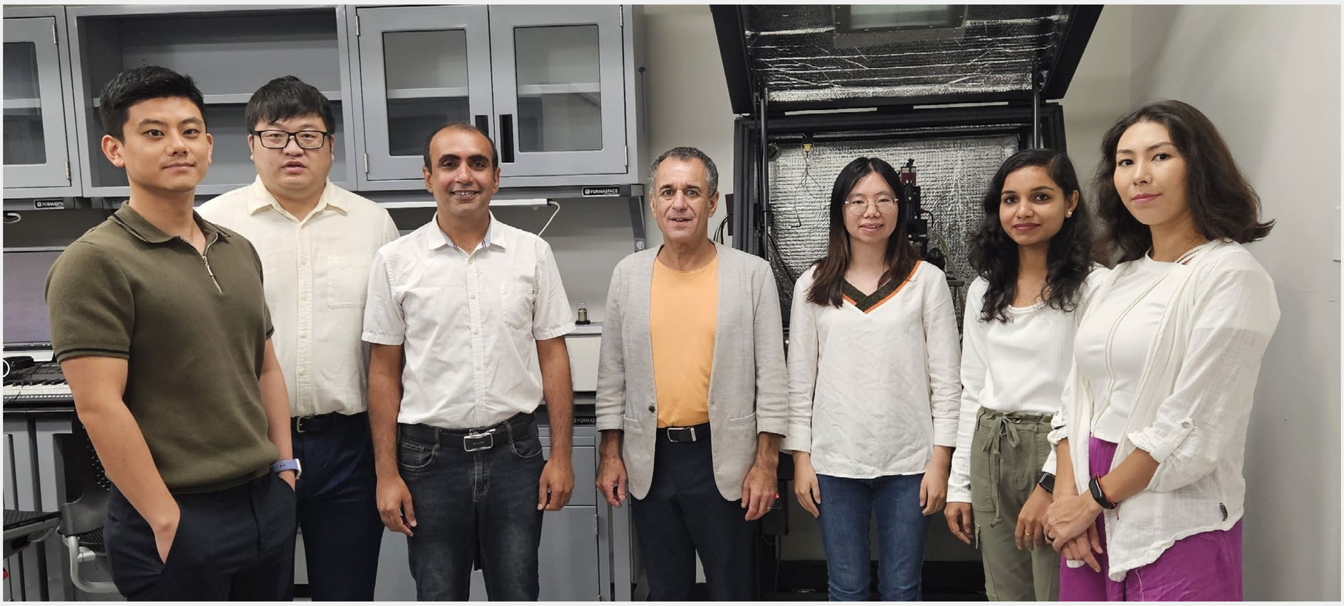

Dr. Michael V. Mirkin is a distinguished chemist and a leading figure in the field of electrochemistry, currently serving as a professor at Queens College, City University of New York (CUNY). Originally from the former USSR, Professor Mirkin earned his BS/MS in Chemistry in 1982 and his PhD in Electrochemistry in 1987 from Kazakh State University. He began his career as a research associate at his alma mater before moving to the United States, where he conducted postdoctoral research with the late Prof. Allen J. Bard at The University of Texas at Austin from 1990 to 1993 and participated in early development of scanning electrochemical microscopy (SECM). Following this, he joined the faculty at Queens College, where he has continued to advance his research and contribute significantly to the field.

Professor Mirkin and his team at CUNY's Department of Chemistry specialize in nano-electrochemistry, focusing on the development and application of nanometer-sized electrochemical probes combined with advanced scanning probe microscopy techniques. Their research aims to explore and understand a wide range of chemical and biological processes at the nanoscale, leveraging the unique versatility and adaptability of these probes. By integrating nano-electrochemistry with complementary optical techniques and transmission electron microscopy, they strive to attain a more comprehensive understanding of complex systems, from heterogeneous charge transfer reactions to the release of extracellular vesicles from living cells. Their work not only advances fundamental science but also lays the groundwork for potential applications in fields like chemical engineering and catalysis, making significant contributions to the broader landscape of nanoscience and technology.

Professor Mirkin, could you provide an overview of your current research at CUNY's Department of Chemistry?

Our research focuses on nano-electrochemistry, specifically using nanometer-sized electrochemical probes in conjunction with scanning probe microscopy techniques to explore various systems and processes at the nanoscale. These nano-electrochemical probes are highly versatile, allowing us to investigate a wide range of phenomena. For example, we can position the tip near the substrate surface to study charge transfer reactions occurring at a nanostructured solid/liquid interface. Alternatively, a tip can be inserted into a biological cell to probe intracellular processes with high spatial resolution. The flexibility and adaptability of these probes make them suitable for studying diverse samples, from nanoparticles to biological systems, providing unique insights into nanoscale behaviors.

You mentioned that nano-electrochemistry often needs to be combined with other techniques to provide a more complete picture. Can you elaborate on how integrating these methods enhances our understanding of nanoelectrochemical systems?

One of the most exciting developments in nano-electrochemistry is the ability to combine it with other analytical techniques to gain a more comprehensive understanding of systems. Traditional electrochemical methods alone often fall short, especially in providing detailed information about the chemical composition or atomic structure of materials. By integrating nano-electrochemistry with spectroscopy, one can learn more about local chemical environments, and by combining it with techniques like transmission electron microscopy (TEM), we can obtain atomic-scale structural information. This multidisciplinary approach allows researchers to create a more complete picture of the systems they study and tackle complex challenges, such as engineering catalytic sites on the nanoscale by correlating structural, chemical, and activity data.

What were the primary challenges in developing quantitative measurement techniques with scanning electrochemical microscopy (SECM), and how did you address these issues?

Developing quantitative measurement techniques based on scanning electrochemical microscopy (SECM) presented several significant challenges. One of the primary issues was ensuring that the measurements obtained with microelectrode and nanoelectrode probes were reliable and reproducible, especially when dealing with extremely small tips that are difficult to visualize. Visualization typically requires advanced techniques like scanning electron microscopy (SEM) or TEM, but even with these, the in-situ positioning and characterization of probes remain complex. The fragility of these small, glass-sealed electrodes adds another layer of difficulty; unlike more robust atomic force microscopy (AFM) probes, SECM tips cannot physically contact surfaces without being damaged. Achieving reproducibility was also challenging because each nanoelectrode is manually crafted and polished, requiring meticulous handling to ensure consistent results. Overcoming these obstacles involved developing better visualization methods, refining the fabrication process, and creating new strategies to interpret data accurately.

When conducting experiments at the nanoscale, what are the key difficulties in visualizing and modeling these processes, and how do you overcome them to ensure accurate interpretation of data?

Modeling electrochemical processes at the nanoscale involves adapting standard electrochemical theories to the unique conditions presented by nanometer-sized probes. While the fundamental principles of diffusion-based theory still apply, modeling becomes more complex when dealing with probes smaller than 10 nanometers, where double-layer effects and electron tunneling come into play. As a small nanoelectrode approaches a conductive surface, tunneling can alter the expected outcomes, necessitating changes in theoretical approaches. Therefore, while the mathematics remains similar for larger nanoelectrodes, understanding what is being modeled is crucial, especially since direct visualization of these tiny systems is often not possible. Accurate modeling requires a blend of computational tools and imaginative thinking to interpret the unseen dynamics of nanoscale systems.

Could you discuss a recent project from your lab that you found particularly novel or interesting, especially in how it advances our understanding of molecular electrocatalysis?

Traditionally, in molecular catalysis, the rate of a bimolecular catalytic reaction is thought to be independent of the applied electrical potential. We have recently developed voltage-driven electrocatalysis, in which a molecular catalyst is immobilized directly (i.e., without a spacer) on the electrode surface, and the applied potential drops on both sides of the attached molecule, driving both the oxidation/reduction of the molecular catalyst and the charge transfer between the catalyst and dissolved reactant species. The electrode potential contribution to the catalytic driving force allows a molecular catalyst to accelerate the rates of charge-transfer processes, which it normally would not be able to catalyze. This finding not only broadens the theoretical understanding of molecular electrocatalysis but also offers new pathways for designing more efficient catalytic systems.

While your research is primarily fundamental, are there any specific examples where your work in nanoscale electrochemistry has influenced or could influence real-world applications or technologies?

Although our primarily focus is on fundamental science, some of our techniques have begun to find applications in real-world scenarios. For instance, SECM and its nanoscale variant, nano-SECM, are gaining traction in chemical and electrochemical engineering fields. Although my lab typically does not engage in industrial collaborations or direct application development, the foundational concepts we have developed are being adapted by engineers and applied researchers to solve practical problems in industry. This progression illustrates the potential of fundamental research to inspire technological innovations, even if the initial work was not directly aimed at application.

Looking to the future, what are some of the emerging challenges or research directions in nanoscale electrochemistry that you are excited to explore?

Looking ahead, our research aims to push the boundaries of what is possible in nanoscale electrochemistry by developing smaller, more precise, and more reliable probes. This goal includes expanding the range of materials and processes we can study, continually refining our techniques, and addressing the new challenges that arise as we push the limits of current technology. A recent focus area is studying photoelectrochemical processes on single semiconductor nanoparticles, which combines the challenges of nanoscale electrochemical measurements with the need for localized illumination. This emerging area requires both new technological developments and innovative approaches to study these complex systems. Our work is dynamic and evolves with each new discovery, driven by the unpredictability and excitement of scientific exploration.

Thank you, Professor Dr. Mirkin, for sharing your valuable insights and discussing your research with us.

Park Atomic Force Microscope

Scanning Electrochemical Cell Microscopy

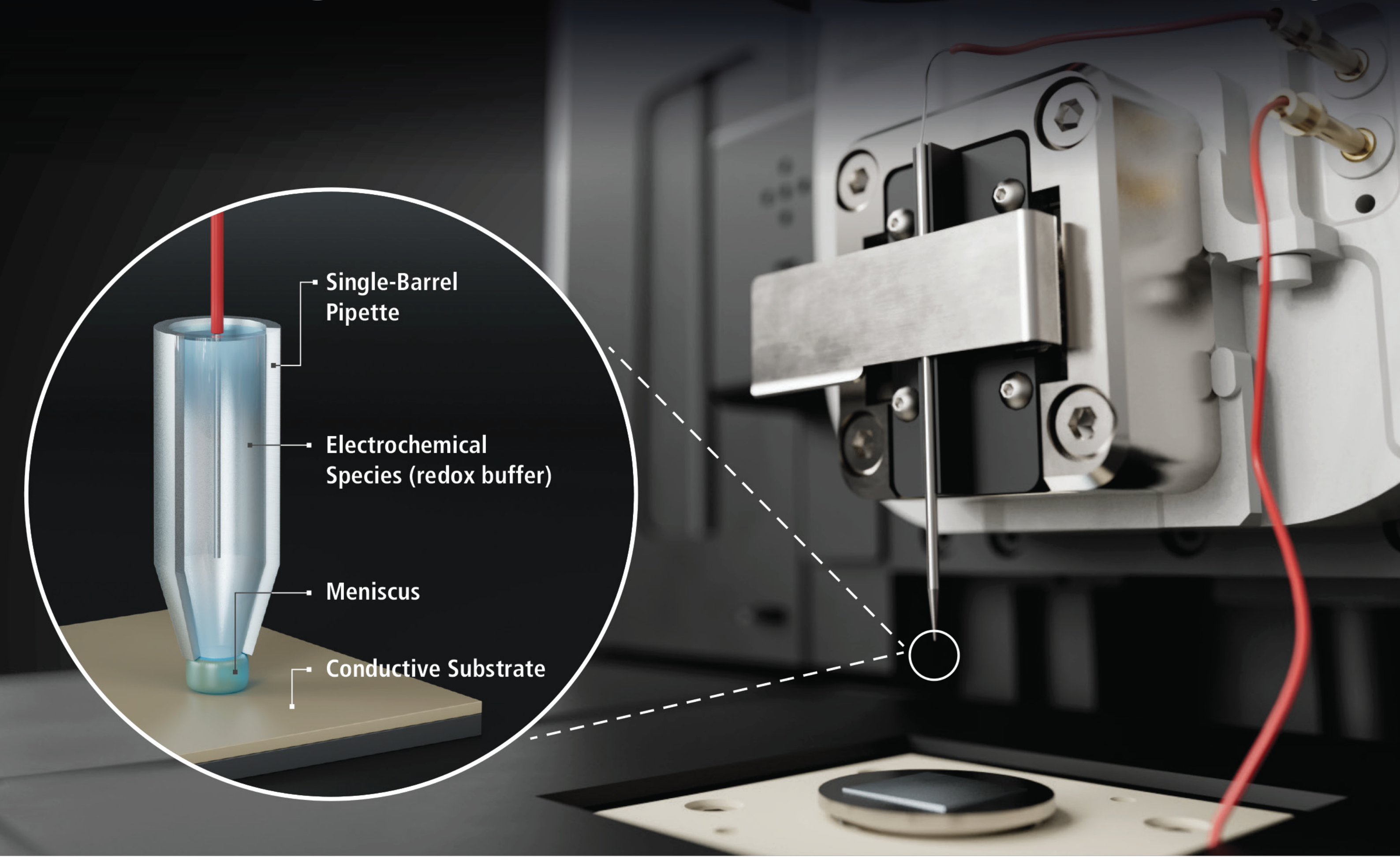

Park SECCM Technology

Introducing a Novel Approach
to Electrochemical Measurement

Gain Deeper Insights into Electrochemical Properties of a Material

- Understand the physical and chemical processes of ion transfer distribution across various electrodes.
- Analyze both conductive and semiconductive substrates with high precision.

Accelerate Fuel Cell Design and Battery Materials Research

- Study the effects and performance of various anode, cathode and electrolyte materials for Lithium-ion batteries.
- Apply to both conventional and solid-state cells.

Unlock the Potential of Nanoscale Surface Modification

- Locally modify substrates under electrochemical control through electrolysis and electrosynthesis.
- Utilize for galvanization, cathodic protection, and anti-corrosion mathods and materials.

Park NX12

Park
SYSTEMS

parksystems.com

PRIMER:
SCANNING ELECTROCHEMICAL CELL MICROSCOPY (SECCM)

Introduction

Interest in surface investigations and the study of chemical properties has been steadily increasing. Electrochemical property research, in particular, holds significant importance in various academic and industrial applications. These applications include studying ion transfer distribution across electrodes [1,2], characterizing anode/cathode materials for battery design [3], modifying substrates for surface enhancement [4,5], assessing metal-oxide corrosion [6,7], and studying single-cell electrochemical activity [8].

While numerous measurement techniques have been developed, pipette-based scanning probe microscopy (SPM) methods offer novel insights into exploring the chemical properties of nanoscale samples. Scanning electrochemical microscopy (SECM) [9], one of the first-generation pipette-based SPMs for electrochemical measurements, greatly contributed to visualizing chemical reactions at interfaces. However, SECM has limitations, such as challenges in controlling the distance between the probe and sample surface and the need to immerse the sample in a liquid medium.

In contrast, scanning electrochemical cell microscopy (SECCM) [10-14] uses an electrolyte-filled nano-pipette to create a meniscus contact at the sample surface, forming an electrochemical cell at the tip of the pipette. Since its inception, SECCM has proven valuable in various research fields due to its ability to provide localized measurements at the nanometer scale, intuitive pipette control, and capability to operate under ambient conditions.

In this primer, we introduce SECCM, including its principles, setup, and diverse applications. Additionally, we explain the interpretation of the cyclic voltammetry (CV) curve recorded by SECCM and the CV mapping image for few-layer graphene deposited on conductive substrates. We discuss the broad utility of SECCM in various fields, demonstrating its potential to significantly advance nanoscale electrochemical research.

SECCM Set-up and Electrochemical Measurements

SECCM utilizes a glass pipette with an inner diameter in the range of hundreds of nanometers for local electrochemical property measurements. To prepare it, a glass pipette (G100F3, Warner Instruments, U.S.A.) with a 1 mm outer diameter (O.D.) and a 0.58 mm inner diameter (I.D.) is pulled using a commercial CO_2 laser pipette puller (P2000, Sutter Instruments, U.S.A.) to fabricate nano-pipettes with an I.D. of approximately 200 to 350 nm (Fig. 1A). An Ag/AgCl electrode, serving as a quasi-reference counter electrode (QRCE), is inserted into the pipette, which is then filled with an electrolyte solution containing 10 mM $Ru(NH_3)_6Cl_3$ and 100 mM KCl. A voltage is applied between the conductive substrate and the pipette electrode filled with the electrolyte solution (Fig. 1B). The probe's approach is controlled using the ionic current: a sharp increase in the ionic current indicates the formation of a meniscus (electrochemical cell). The distance between the pipette end and the sample is determined by the meniscus formed between them. As the pipette, with a hemisphere-shaped bubble of solution at the end, approaches the sample vertically, the meniscus forms between the pipette end and the sample surface, creating a closed electrical circuit that causes a sharp ionic current spike. This signal is used to halt the pipette's approach and maintain a constant distance between the pipette and the sample [10], [12].

To visualize the electrochemical signal, approach-retract scanning (ARS, also known as hopping mode) is utilized. This method involves the approach of the nano-pipette, followed by CV curve determination, retraction of the nano-pipette, and its lateral movement. At each point, an independent CV curve is measured. CV mapping uses a series of predefined locations in a grid (Fig. 2) to build its images.

SECCM CV mapping process. The EC response contrast of the sample surface is displayed as an image with a cycle of repeated approach-CV curve measurement-retract-lateral movement.

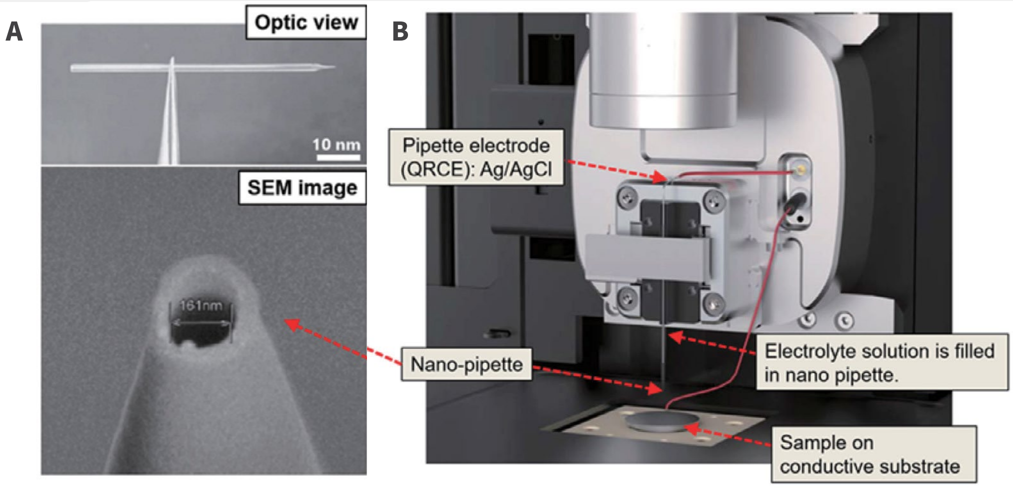

Fig. 1. Images of pulled nano-pipette with ~161 nm I.D. (A) and Park Systems SECCM set-up including parts description. (B) A voltage is applied between the conductive substrate and the pipette electrode filled with the electrolyte solution.

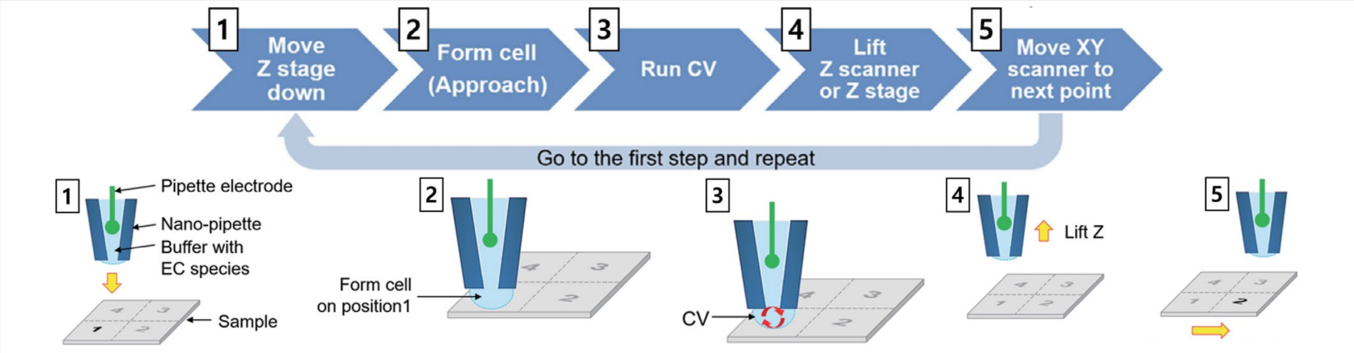

Fig. 2. SECCM CV mapping process. The EC response contrast of the sample surface is displayed as an image with a cycle of repeated Approach-CV curve measurement-Retract-Lateral movement.

Cyclic Voltammetry

Cyclic voltammetry (CV) is a widely used electrochemical technique that involves applying a varying potential to an electrochemical cell while measuring the resulting current. It provides information about the redox behavior and electrochemical properties of a system, such as the oxidation and reduction potentials, electron transfer kinetics, and diffusion coefficients of electroactive species [15].

In a typical CV experiment, a working electrode is immersed in an electrolyte solution and connected to a potentiostat, which applies a potential ramp to the working electrode. The potential is scanned linearly with respect to time, and the resulting faradaic current is measured. The potential ramp can be either positive or negative, and the direction of the scan is reversed periodically to create a "cyclic" pattern. The measured current is plotted against the applied potential to generate a cyclic voltammogram, which is a graphical representation of the electrochemical behavior of the system under study. The resulting voltammogram typically exhibits peaks or waves corresponding to the oxidation and reduction of electroactive species present in the electrolyte solution.

CV curves obtained in SECCM can exhibit different types, each carrying specific meanings and providing insights into the electrochemical behavior of the sample. For example, CV curves on highly oriented pyrolytic graphite (HOPG) with 10 mM $Ru(NH_3)_6Cl_3$ and 100 mM KCl were recorded.

Steady-state CV curve (Fig. 3A): The current response at the working electrode stabilizes at a constant or near-constant value after several scan cycles. This indicates that the electrochemical system has reached a steady state, where the rates of oxidation and reduction reactions are balanced, and the current response has achieved stable, reproducible behavior. In a steady-state CV curve, species concentrations remain constant over time at any point along a curve and only vary with distance from the electrode.

Reversible (Quasi-Reversible) CV curve (Fig. 3B): This type of CV curve typically exhibits well-defined anodic and cathodic peaks of equal height and shape, and the current response returns to the baseline between the peaks. This indicates a reversible or quasi-reversible redox process, where electron transfer is rapid, and the species undergoing oxidation and reduction have similar kinetics.

Irreversible CV curve (Fig. 3C): In this type of CV curve, the anodic and cathodic peaks are asymmetric. The current response does not return to the baseline between the peaks, indicating that the electron transfer is slow or involves chemical reactions. The peak potentials provide information about the redox potentials of the species, but due to the slow electron transfer or involvement of chemical reactions, the peak currents may not accurately reflect the concentration of the electroactive species.

The voltage scan rate plays a crucial role in the shape and characteristics of the CV curve. Changes in the scan rate can result in changes in the shape, size, and peak potential of the CV curve. The scan rate affects the rate of electron transfer reactions that occur at the electrode surface. A higher scan rate typically leads to faster electron transfer kinetics, resulting in changes in the shape and magnitude of the CV curve. Fig. 4 shows how the current signal was affected by the scan rate of the CV curves. To evaluate the effect of scan rate, CV curves on HOPG with 10 mM $Ru(NH_3)_6Cl_3$ and 100 mM KCl and a ~340 nm I.D. nano-pipette were performed using a range of scan rates (0.1 to 10 V/s). As shown in Fig. 4, the CV curve peak current increased as a function of scan rate. Theoretically, as the scan rate increases, the peak current increases, and the peak-to-peak potential also increases [12], [16].

At scan rates below 1 V/s, the peak current values decreased slightly and ranged from -65 pA to -72 pA. In contrast, at scan rates above 1 V/s, especially from 3 to 10 V/s, the response

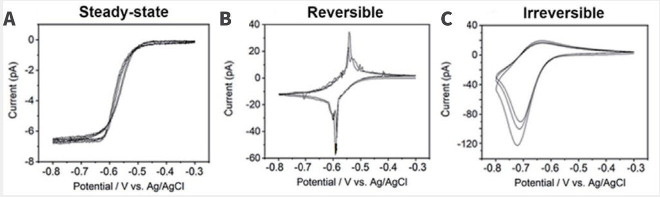

Fig. 3. Types of CV curve, steady-state (A), reversible (B), and irreversible (C).

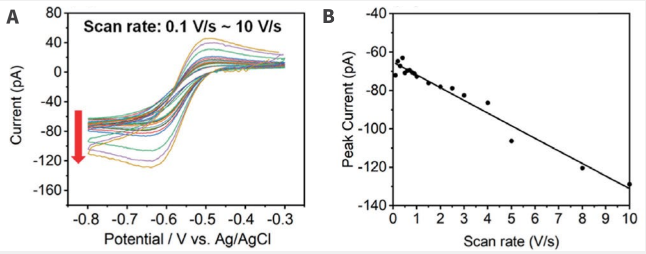

Fig. 4. CV curves (A) and peak currents as a function of different scan rates (0.1 V/s to 10 V/s). (B) As the scan rate increases, the peak current also increases. This was performed using a 340 nm inner diameter nano-pipette with an aqueous solution containing 10 mM $Ru(NH_3)_6Cl_3$ and 100 mM KCl on HOPG.

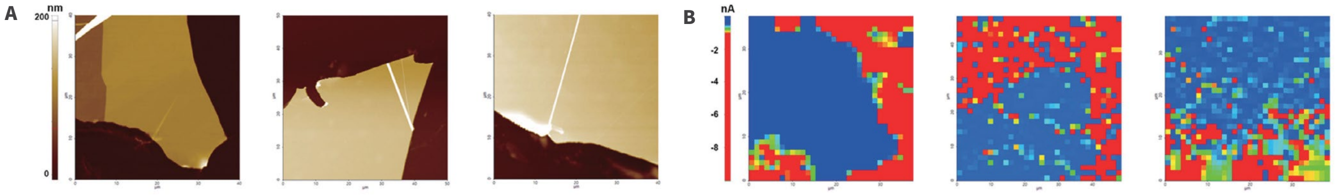

Fig. 5. AFM height images (A) and CV mapping images on graphene flakes on an ITO substrate sample (B) Different EC responses on graphene flakes and the ITO substrate were clearly confirmed on the CV mapping image. Each CV curve was performed using ~340 nm of I.D. nano-pipette with an aqueous solution containing 10 mM $Ru(NH_3)_6Cl_3$ and 100 mM KCl, and the scan rate was 1 V/s.

began to show the peak expected for linear diffusion, and the peak current increased to -130 pA. Although the CV curve displayed a somewhat peak-shaped form, the steady-state component still dominated as indicated by the current value at the switching potential and the small peak current ratio.

Next, we obtained AFM images to determine surface morphologies and CV mapping to estimate EC signal contrasts on few layers graphene deposited on an indium tin oxide (ITO) substrate. All CV mapping images were obtained using a ~340 nm I.D. nano-pipette, 10 mM $Ru(NH_3)_6Cl_3$, 100 mM KCl supporting electrolyte, and a 1 V/s scan rate. Using confined meniscus contact, nano-scale imaging can distinguish the EC signal of the graphene basal plane, multi-layered graphene, and graphene with a conductive substrate. Heights from 50 to 100 nm were found at graphene multi-layers by AFM and a significantly clear EC signal contrast was recognized by CV mapping. Higher EC response can be attributed to the ITO substrate, so graphene flakes showed lower EC currents compared to the ITO substrate.

Conclusion

In this primer, we have highlighted the successful application of SECCM by Park Systems in measuring faradaic current signals and accurately reading potential in the presented data set. The accuracy of potential reading is critical in electrochemistry, as it determines reaction efficiency, which is essential for practical applications such as catalyst development, even in fundamental research.

SECCM is a powerful technique for studying local electrochemical properties at the nanoscale using pipette-based scanning electrochemical microscopy. It offers advantages such as intuitive pipette control, ambient condition measurement, and the ability to perform local measurements with high spatial resolution. By interpreting CV curves and CV mapping images, SECCM provides valuable insights into the electrochemical behavior of samples. This technique has been widely used in various research fields, including the study of ion transfer distribution, battery materials, surface modification, metal-oxide corrosion, and single-cell electrochemical activity.

With its unique capabilities, SECCM continues to contribute to the growing interest in surface investigations and chemical properties, opening new possibilities for nanoscale electrochemical research.

References

1. Patten, H. V., Lai, S. C. S., MacPherson, J. V. & Unwin, P. R. Active sites for outer-sphere, inner-sphere, and complex multistage electrochemical reactions at polycrystalline boron-doped diamond electrodes (pBDD) revealed with scanning electrochemical cell microscopy (SECCM). Anal. Chem. 84, 5427–5432 (2012).
2. G. Güell, A., Ebejer, N., E. Snowden, M., V. Macpherson, J. & R. Unwin, P. Structural Correlations in Heterogeneous Electron Transfer at Monolayer and Multilayer Graphene Electrodes. J. Am. Chem. Soc. 134, 7258–7261 (2012).
3. Ruffo, R., Wessells, C., Huggins, R. A. & Cui, Y. Electrochemical behavior of LiCoO2 as aqueous lithium-ion battery electrodes. Electrochem. commun. 11, 247–249 (2009).
4. Kooi, S. E., Schlecht, U., Burghard, M. & Kern, K. Electrochemical modification of single carbon nanotubes. Angew. Chemie - Int. Ed. 41, 1353–1355 (2002).
5. G. Williams, C., A. Edwards, M., L. Colley, A., V. Macpherson, J. & R. Unwin, P. Scanning Micropipet Contact Method for High-Resolution Imaging of Electrode Surface Redox Activity. Anal. Chem. 81, 2486–2495 (2009).
6. Leidheiser, H. Electrical and Electrochemical Measurements As Predictors of Corrosion At the Metal-Organic Coating Interface. Prog. Org. Coatings 7, 79–104 (1979).
7. Suter, T. & Böhni, H. Microelectrodes for studies of localized corrosion processes. Electrochim. Acta 43, 2843–2849 (1998).
8. Pan, R., Xu, M., Jiang, D., Burgess, J. D. & Chen, H. Y. Nanokit for single-cell electrochemical analyses. Proc. Natl. Acad. Sci. U. S. A. 113, 11436–11440 (2016).
9. Bard, A. J., Fan, F. F., Kwak, J. & Lev, O. Scanning Electrochemical Microscopy. Introduction and Principles. 61, 132–138 (1989).
10. Ebejer, N., Schnippering, M., Colburn, A. W., Edwards, M. A. & Unwin, P. R. Localized high resolution electrochemistry and multifunctional imaging: Scanning electrochemical cell microscopy. Anal. Chem. 82, 9141–9145 (2010).
11. Snowden, M. E. et al. Scanning electrochemical cell microscopy: Theory and experiment for quantitative high resolution spatially-resolved voltammetry and simultaneous ion-conductance measurements. Anal. Chem. 84, 2483–2491 (2012).
12. Ebejer, N. et al. Scanning Electrochemical Cell Microscopy: A Versatile Technique for Nanoscale Electrochemistry and Functional Imaging. Annu. Rev. Anal. Chem. 6, 329–351 (2013).
13. Bentley, C. L., Kang, M. & Unwin, P. R. Scanning electrochemical cell microscopy: New perspectives on electrode processes in action. Current Opinion in Electrochemistry vol. 6 23–30 (2017).
14. Daviddi, E., Gonos, K. L., Colburn, A. W., Bentley, C. L. & Unwin, P. R. Scanning Electrochemical Cell Microscopy (SECCM) Chronopotentiometry: Development and Applications in Electroanalysis and Electrocatalysis. Anal. Chem. 91, 9229–9237 (2019).
15. Costentin, C., Fortage, J. & Collomb, M.-N. Electrophotocatalysis: Cyclic Voltammetry as an Analytical Tool. J. Phys. Chem. Lett. 11, 6097–6104 (2020).
16. Zhang, G., Cuharuc, A. S., Güell, A. G. & Unwin, P. R. Electrochemistry at highly oriented pyrolytic
graphite (HOPG): lower limit for the kinetics of outer-sphere redox processes and general implications for electron transfer models. Phys. Chem. Chem. Phys. 17, 11827–11838 (2015).

PRUSSIAN BLUE NANOFILM-SENSITIZED PLASMONIC ELECTROCHEMICAL MICROSCOPY FOR SPATIALLY RESOLVED DETECTION OF THE LOCALIZED DELIVERY OF HYDROGEN PEROXIDE

Adaly Garcia, Christina Dhoj, Samuel Groysman, Kinsley Wang, Stellina Ao, Aimee Anguiano, Tony Tran, Dianlu Jiang, Yixian Wang* Department of Chemistry and Biochemistry, California State University, Los Angeles, Los Angeles, CA, USA

This article has been condensed by NanoScientific from the original publication in Elsevier B.V., published online on 26 June 2024, under a Creative Commons Attribution 4.0 International License. This summary aims to provide a shorter and more accessible version of the article. To read the full original article, please visit https://doi.org/10.1016/j.snr.2024.100218.

ABSTRACT

This study introduces a novel Prussian blue (PB) nanofilm-sensitized plasmonic electrochemical microscopy (PEM) technique for real-time, spatially resolved detection of hydrogen peroxide (H_2O_2). The PB nanofilm, characterized and tested in amperometric mode, effectively visualizes localized H_2O_2 delivery. Using a micropipette to create and monitor a concentration gradient on the sensor surface, the technique demonstrated precise detection, further validated by numerical simulations. This method holds promise for applications in biomedical research, such as analyzing single-cell exocytosis of neurotransmitters like dopamine, with potential improvements in film uniformity expected to enhance resolution.

Introduction

Traditional electrochemical (EC) techniques typically measure averaged responses from a collection of microstructures, mesoscopic substances, ions, and molecules . While effective for bulk analysis, these approaches often overlook the inherent complexity and heterogeneity of many systems, highlighting the need for EC methodologies capable of spatially resolved detection. Advancements in this area have led to various scanning probe-based imaging methods, such as scanning electrochemical microscopy (SECM) and scanning electrochemical cell microscopy (SECCM), as well as adaptations of optical techniques, including fluorescence, plasmonic , dark field , and Raman scattering microscopy . Scanning probe techniques offer high spatial resolution but often lack temporal resolution, whereas optical methods provide excellent temporal resolution but with reduced spatial information [1-9].

Plasmonic electrochemical microscopy (PEM) emerges as a powerful technique that uses surface plasmon resonance (SPR) on metallic nanofilm electrodes, such as gold or silver, to achieve spatially resolved detection at scales beyond conventional EC approaches . PEM captures local changes due to EC processes on the electrode surface, where plasmonic signals are linked to bulk refractive index changes, dielectric property alterations, redox molecular binding, or EC-induced deposition near the metal film. This microscopy feature enables detailed spatial analysis of electrochemical activities on the electrode [10-22].

In this study, we present a significant advancement in PEM by introducing a "dye-sensitized" approach, termed DS-PEM. This method enhances sensitivity while maintaining precise spatial resolution by coating the PEM sensor with a redox-active dye, which changes color during specific electrochemical reactions, intensifying the optical signals detected by PEM. The technique's model application is the detection of hydrogen peroxide (H_2O_2), a key biomarker in various physiological processes . Conventional electrochemical assays like amperometry, voltammetry, and impedance spectroscopy are commonly used for H_2O_2 detection but often lack spatial resolution. Previous spatially resolved detection methods, including microsensor arrays , SECM , and fluorescent imaging , face challenges such as low throughput, laborious protocols, and dependence on fluorescent labeling. [23-29].

The DS-PEM approach addresses these issues by utilizing a Prussian blue (PB) nanofilm as a sensing layer on the PEM chip, building on earlier work that demonstrated the efficacy of Prussian blue nanoparticles (PBNPs) in H_2O_2 detection via catalytic reduction. In the presence of H_2O_2 , the PB-to-Prussian white (PW) conversion is limited, reducing the refractive index change and the corresponding PEM signal. This inverse correlation allows for a reliable measurement of H_2O_2 levels. We applied a uniform PB film to the PEM sensor to achieve sensitive, spatially resolved H_2O_2 detection. The localized H_2O_2 delivery was simulated using a micropipette, and the resulting micro-scale distributions were mapped using DS-PEM, with accuracy validated through numerical simulations. This technique has the potential to become a crucial tool for precise, spatially resolved electrochemical analysis [21, 30].

Experimental Section

Chemicals and Materials

Ferric chloride, hydrochloric acid, hydrogen peroxide, and other chemicals were purchased from Fisher Scientific (Waltham, MA, USA) and used without further purification. Solutions were prepared using double-deionized water from a Milli-Q Ultrapure water system (MilliporeSigma, Burlington, MA, USA). Silicon wells were cut from flexiPERM reusable silicon inserts (Sarstedt, Germany). Electrodes and sensing chips, including gold-coated glass coverslips (18 mm × 18 mm), were obtained from Biosensing Instruments (Tempe, AZ, USA).

Preparation and Characterization of the Prussian Blue Nanofilm

Prussian blue (PB) nanofilms were prepared by depositing Prussian blue nanoparticles (PBNPs) onto cleaned, gold-coated sensing chips. The PBNPs were synthesized by stirring a mixture of potassium ferrocyanide and ferric chloride, and the solution was applied to the sensing chips, followed by overnight baking at 100°C to form a uniform nanofilm.

The surface morphology of the prepared chips was analyzed using atomic force microscopy (AFM). This analysis was conducted in non-contact air mode on a Park NX12 multifunctional microscopy platform (Park Systems, Suwon, South Korea), which is equipped with a detachable AFM head and non-contact cantilevers (PPP-NCHR, 42 N/m, 330 kHz). The instrument was operated using Smart Scan software, and the AFM images captured were processed with XEI software, both provided by Park Systems, Suwon, South Korea. Before determining the surface roughness, all images were first-order flattened. The roughness was measured as the root-mean-square deviation of z-heights across the surface within 1 µm × 1 µm sections.

Cyclic voltammetry (CV) was performed using a CHI760E potentiostat (CH Instruments, Austin, TX, USA), showing expected redox behavior of the PB film. Plasmonic CVs were recorded using the surface plasmon resonance microscopy (SPRm) system from Biosensing Instruments, matching the electrochemical CVs and confirming selectivity for Faradaic processes.

Instrument Setup

PEM experiments were conducted using a surface plasmon resonance microscopy system (SPRm 200 Series, Biosensing Instruments) integrated with a CHI760E potentiostat (CH Instruments, Austin, TX, USA). The electrochemical cell used a three-electrode setup, with the gold-coated sensing chip as the working electrode. See illustration Scheme 1.

For spatially resolved sensing, H_2O_2 was locally delivered using a micropipette controlled by a TRIO/MP-245A Micromanipulator System (Sutter Instrument, Novato, CA, USA). The distance between the micropipette and the sensor surface was carefully monitored, and P-polarized light was directed onto the chip to induce plasmonic excitations, with reflected light intensity captured by an SPR detector.

Data Processing

Raw plasmonic images were processed using ImageJ and MATLAB. Data from amperometry tests were background-subtracted and normalized, while cyclic voltammetry data were analyzed by calculating the first-order derivative. Results were based on relative plasmonic signal intensities without converting them to current density values.

Numeric Simulations

Numeric simulations were performed in COMSOL Multiphysics 6.0 to model H_2O_2 diffusion from the micropipette to the electrode surface. The simulations, which used the “transport of diluted species” module, closely matched the experimental results, validating the accuracy of the technique.

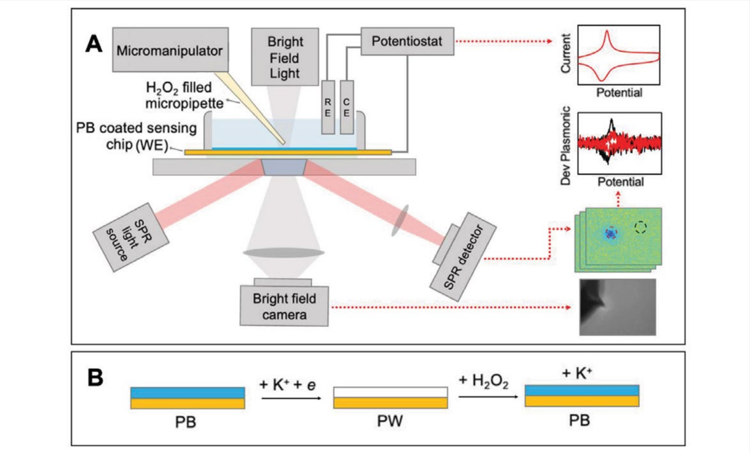

Scheme 1. (A) Schematic of the DS-PEM setup and corresponding data visualization; (B) Reaction mechanism at the PB film.

Results and Discussions

Characterization of Prussian Blue Nanofilms

The PB nanofilms were characterized using SEM-EDS, confirming the presence of carbon, iron, and nitrogen, which are indicative of PB's composition (Figs. 1A–C). ATR-FTIR analysis revealed a sharp band at 2075 cm^{-1}, corresponding to the cyanide group (Fig. 1G). AFM analysis showed a surface roughness of 9.1 ± 0.9 nm (Figs. 1D–E), with a film thickness of 26 ± 3 nm (Fig. 1F). Electrochemical performance was assessed using cyclic voltammetry (CV), which demonstrated expected redox behavior (Fig. 1H). The plasmonic CV, derived from PEM, matched the electrochemical CV, confirming high selectivity for Faradaic processes (Fig. 1I).

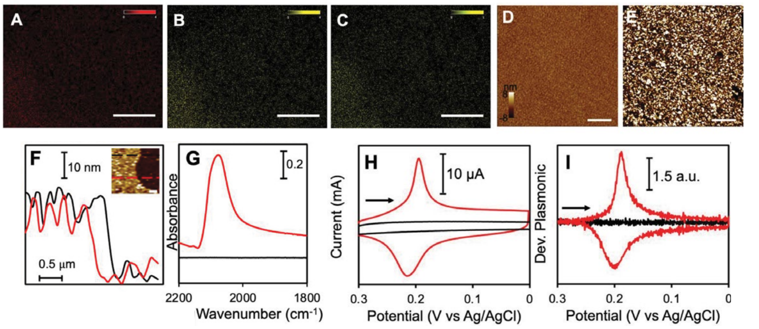

Fig. 1. Comprehensive Characterization of PB Nanofilm on a Sensing Chip. (A-C) SEM-EDS elemental mapping of carbon (A), iron (B), and nitrogen (C) confirms the nanofilm's chemical composition. (D-F) AFM images comparing a bare sensing chip (D) with a PB nanofilm-coated chip (E), and height profiles (F) at the film boundary. Scale bars: 1 µm for A-E and 0.5 µm for F. Images were first-order flattened using XEI. The inset in (F) shows height profile extraction points, with an average film height of 26 ± 3 nm from three measurements. (G) ATR-FTIR spectra of the PB nanofilm (red) and bare chip (black), highlighting the cyanide peak at 2075 cm^{-1}. (H, I) Electrochemical analysis with potentiostat CVs from the whole electrode (~0.9 cm^2) (H) and plasmonic CVs averaged from the sensing area (600 µm × 450 µm, 0.27 mm^2) (I) for PB-modified (red) vs. bare chips (black) at a 0.05 V/s scan rate in 1 M KNO_3.

Sensing Capability of PB Nanofilm-Sensitized PEM

The PB nanofilm's ability to sense H_2O_2 was tested using amperometry under a constant potential. Plasmonic images showed a decrease in intensity with increasing H_2O_2 concentration, indicating the catalytic reduction of H_2O_2 (Figs. 2A–D). Fig. 2F shows the cumulative plasmonic signal from twelve injections, averaged across the sensing area, highlighting its concentration dependence. The plasmonic signal displayed a linear relationship with H_2O_2 concentration (Fig. 2G), whereas

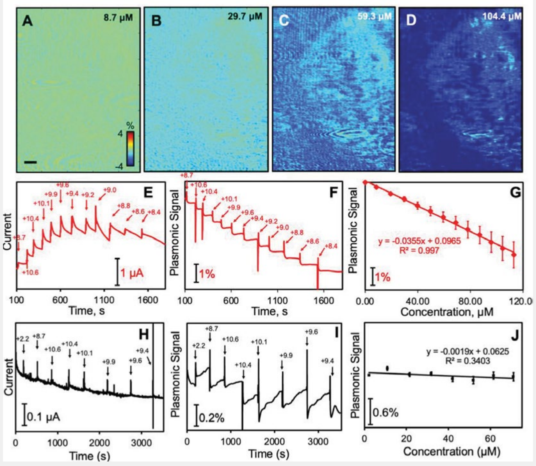

Fig. 2. Amperometric Detection of H_2O_2 Using PB Nanofilm-Sensitized PEM. (A-D) PEM snapshots of the nanofilm at varying H_2O_2 concentrations under a −0.1 V bias, taken before each subsequent injection. Scale bar: 50 μm. (E-J) Real-time data from the potentiostat (E, H) and PEM (F, I), with calibration curves correlating PEM signal intensity to H_2O_2 concentration (G, J), are shown for both a nanofilm-coated chip (E-G) and a bare chip (H-J). In F and I, PEM signals are averaged over the entire imaged area (600 μm × 450 μm, 0.27 mm^2), while G and J present mean ± standard deviation data from 88 regions of interest (ROIs), each approximately 54 μm × 54 μm. Numbers in E, F, H, and I indicate H_2O_2 concentrations in μM, considering dilution factors.

the potentiostat current lacked this correlation at higher concentrations (Fig. 2E). The calibration curve derived from 88 regions of interest (ROIs) exhibited strong linearity ($R^2 = 0.997$), confirming the consistency of the PEM signals for calculating H_2O_2 concentrations. Comparatively, the signals from bare sensing chips were much weaker and less reliable (Figs. 2H–J).

Spatially Resolved Detection of Locally Delivered H_2O_2

A micromanipulator system controlled the precise delivery of H_2O_2 via a micropipette, creating a localized concentration gradient on the sensor surface. Heatmaps generated from PEM images tracked the formation and growth of this gradient as the micropipette approached the sensor (Figs. 3A–E). Concentration profiles extracted from these heatmaps confirmed effective H_2O_2 delivery and spatial resolution (Figs. 3G, 3H). Real-time concentration variations were observed, with significant increases in the deposition spot (Fig. 3G).

The spatial concentration distributions showed clear gradients correlating with the micropipette's distance from the sensor (Figs. 3N–O). Plasmonic cyclic voltammograms (CVs) further validated that the presence of H_2O_2 resulted in a smaller signal increase at the delivery spot compared to the background (Figs. 3J–K). Numerical simulations using COMSOL Multiphysics supported these experimental results, showing a strong correlation between simulated and observed H_2O_2 concentrations (Figs. 3L–M).

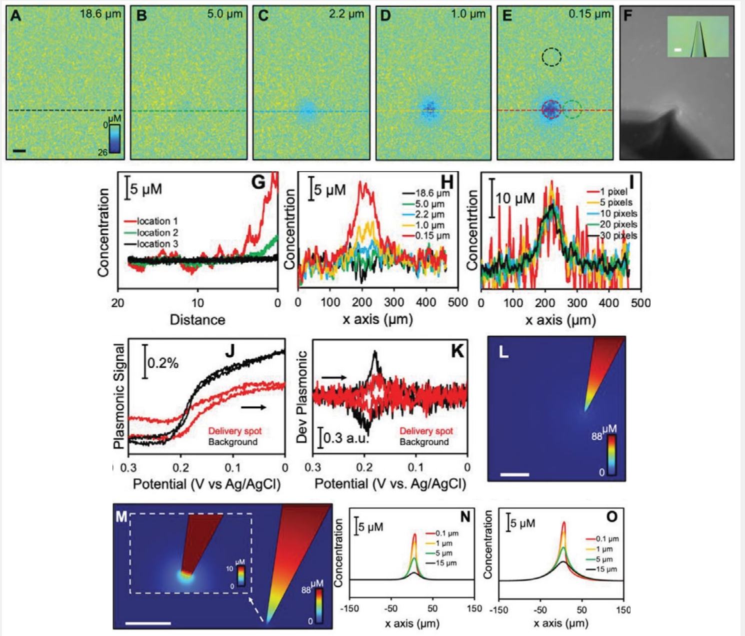

Fig. 3. Spatially Resolved Detection of Locally Delivered H_2O_2 Using PB Nanofilm-Sensitized PEM. (A-E) Heatmaps showing H_2O_2 concentrations at the sensing surface during micropipette approaches under a −0.1 V bias. Scale bar: 50 μm. Concentrations were determined using the calibration from Fig. 2. (F) Optical image of the micropipette's position post-approach, with an inset showing the pipette before use. Scale bar: 20 μm. (G) Distance-dependent concentration traces from specific ROIs marked by dashed circles in E. (H) Concentration profiles along the x-axis across the delivery site from A-E, averaged over a 20-pixel span (~20 μm) along the y-axis, at varying micropipette-to-sensor distances. (I) Concentration profiles along the x-axis at a fixed micropipette-to-sensor distance of 0.15 μm, averaged over different pixel counts along the y-axis. (J, K) Comparative plasmonic cyclic voltammograms at the delivery spot (red) versus an unaffected background area (black), shown before (J) and after taking the time derivative of the plasmonic signal (K). (L-O) COMSOL-simulated concentration profiles: 2D distribution of H_2O_2 diffusion from the micropipette at distances far from (L) and near (M) the sensor surface (scale bar: 50 μm), and longitudinal concentration profiles across the delivery site at 0.1 s (N) and 1 s (O) after loading the micropipette with a pre-set concentration gradient.

Conclusions

We successfully developed a novel Prussian blue (PB) nanofilm-sensitized plasmonic electrochemical microscopy (PEM) technique for precise, spatially resolved detection of hydrogen peroxide (H_2O_2). The PB nanofilm was carefully annealed onto the sensing chip, and its ability to detect H_2O_2 was validated in amperometric mode, showing a clear correlation between the plasmonic signal and H_2O_2 concentration. By integrating a micromanipulator system, we achieved localized delivery of H_2O_2, enabling detailed mapping of concentration gradients at the micrometer scale. The accuracy of the PEM technique was further confirmed through numerical simulations, establishing its potential as a powerful tool for exploring localized electrochemical activities. Given PB's proven effectiveness in catalyzing dopamine, this technique holds significant promise for advancing research in single-cell exocytosis, particularly in studying neurotransmitters like dopamine. Overall, our work extends the applications of PB-sensitized PEM and represents a significant step forward in electrochemical sensing, with promising implications for future bioanalytical research.

REFERENCES AND SUPPLEMENTARY MATERIALS

Supplementary material associated with this article and list of references can be found at https://doi.org/10.1016/j.snr.2024.100218

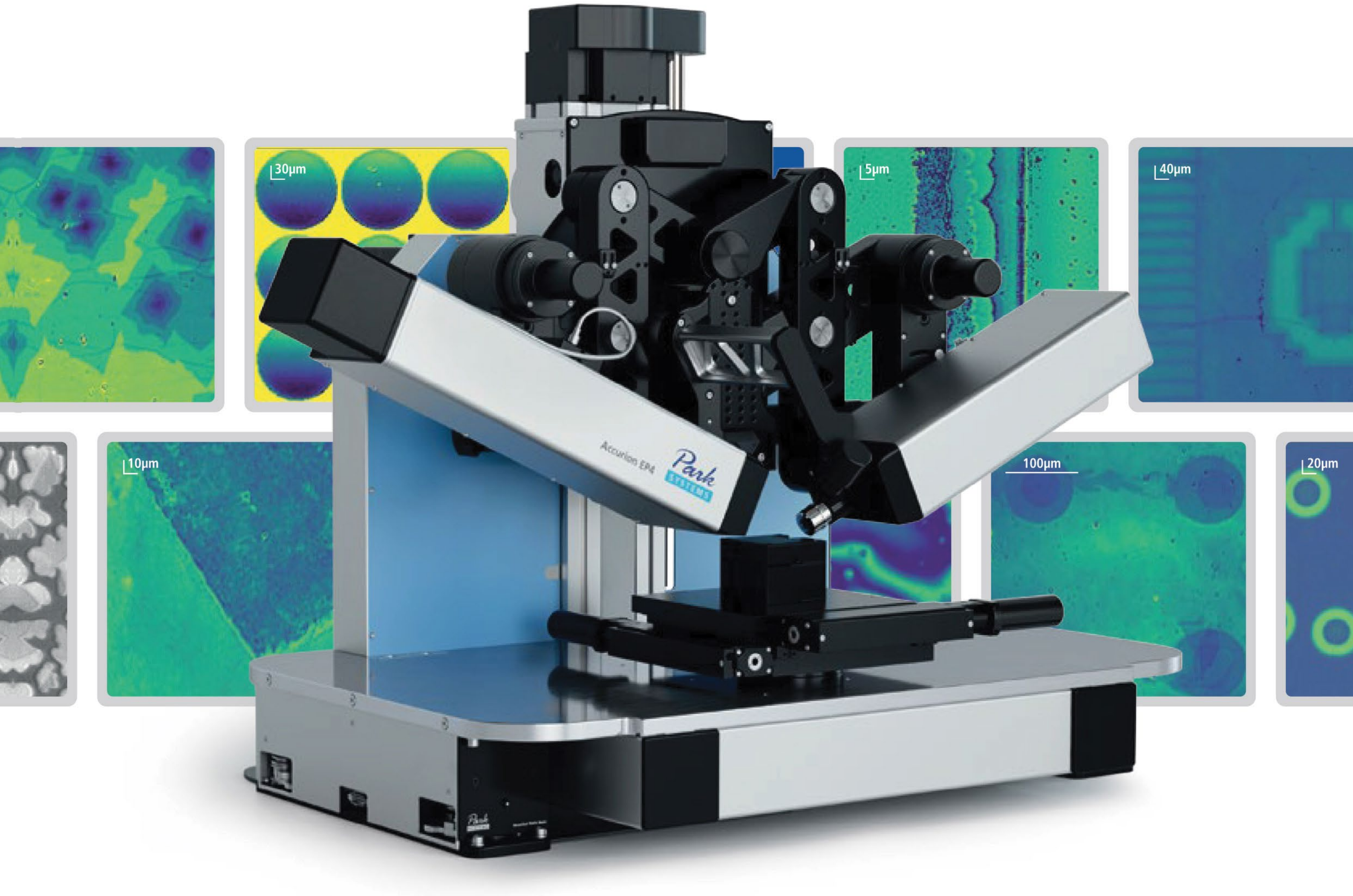
30µm
5µm
40µm
10µm
100µm
20µm
Accurion EP4
Park SYSTEMS

ANOMALOUS INTERFACIAL ELECTRON-TRANSFER KINETICS IN TWISTED TRILAYER GRAPHENE CAUSED BY LAYER-SPECIFIC LOCALIZATION

Kaidi Zhang, Yun Yu, Stephen Carr, Mohammad Babar, Ziyan Zhu, Bryan Junsuh Kim, Catherine Groschner, Nikta Khaloo, Takashi Taniguchi, Kenji Watanabe, Venkatasubramanian Viswanathan, and D. Kwabena Bediako*

This article has been condensed by NanoScientific from the original publication in ACS Central Science, 2023, 9(6), 1119–1128, published on May 15, 2023, under a Creative Commons Attribution 4.0 International License. This summary aims to provide a shorter and more accessible version of the article. To read the full original article, please visit https://doi.org/10.1021/acscentsci.3c00326.

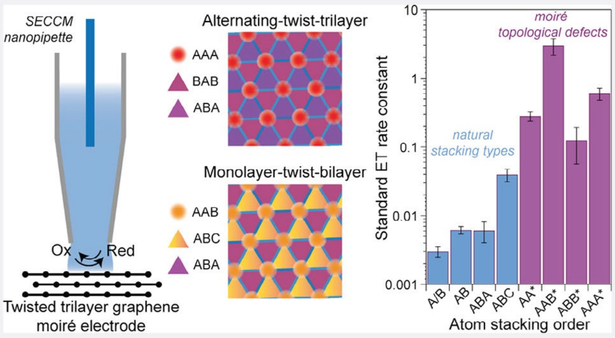

ABSTRACT

Interfacial electron-transfer (ET) reactions are fundamental to converting electrical energy into chemical energy and vice versa. The electronic state of electrodes significantly affects ET rates due to variations in the electronic density of states (DOS) among metals, semimetals, and semiconductors. In this study, we demonstrate that by adjusting interlayer twists in well-defined trilayer graphene moirés, ET rates depend heavily on electronic localization within each atomic layer rather than the overall DOS. The high tunability of moiré electrodes results in local ET kinetics varying by up to three orders of magnitude across different three-layer configurations, surpassing rates observed in bulk metals. Our findings highlight that electronic localization, beyond ensemble DOS, is crucial for interfacial ET, offering insights into the high reactivity often seen at electrode-electrolyte interface defects.

Introduction

Electron-transfer (ET) reactions at electrode-electrolyte interfaces are crucial for electrochemical energy conversion. The electronic structure of electrodes, described by theories such as the Marcus-Gerischer formalism and the Marcus-Hush-Chidsey (MHC) model, influences ET rates. Recent studies show the importance of local density of states (DOS) in understanding interfacial ET kinetics, especially in semiconductor or semimetallic electrodes where atomic defects like vacancies and step edges enhance interfacial reactivity.

Azimuthal misalignment in atomically thin layers creates moiré superlattices, altering the electronic band structure depending on the interlayer twist angle. These structures, particularly at specific "magic" angles, form flat electronic bands with high DOS localized in real space. This has been observed in small-angle twisted bilayer graphene (TBG), where ET kinetics can be tuned by varying the twist angle (θ_m) between 0° to 2°.

The stacking order in multilayer graphene significantly affects its electronic properties. Bernal (ABA-stacked) trilayer graphene has dispersive bands, while rhombohedral (ABC) graphene has flat bands near the Fermi level, leading to correlated electron phenomena at low temperatures. Twisted trilayer graphene (TTG) structures, like monolayer-twist-bilayer (M-t-B) and A-t-A (alternating-twist-angle) heterostructures, exhibit extremely flat bands at magic angles around 1.5°.

These flattened bands create high DOS localized on AAB and AAA sites in M-t-B and A-t-A TTG, respectively, offering unique opportunities to study how electronic structure influences interfacial ET (Fig. 1). For example, larger DOS in A-t-A compared to M-t-B near their magic angles might correlate with higher ET rates based on the MHC model.

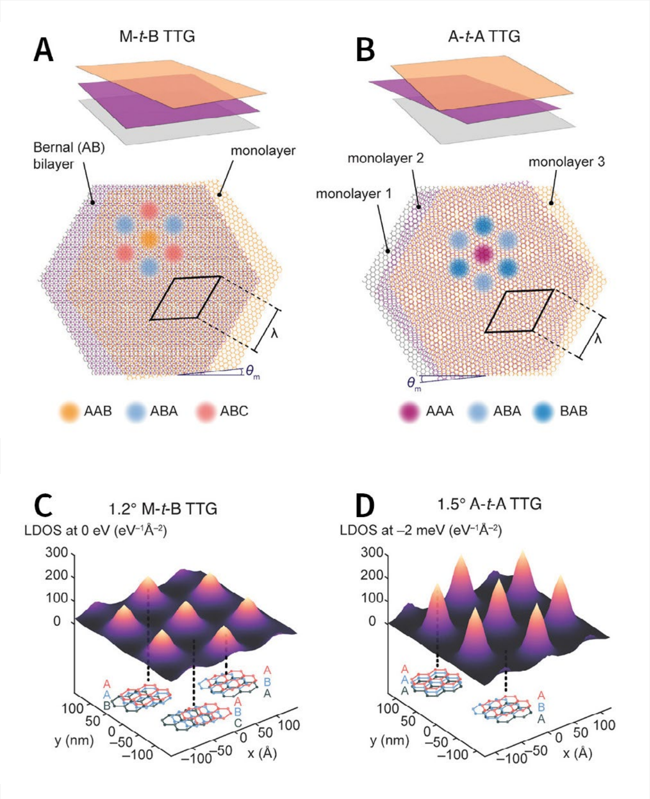

Fig. 1. Polytypes of twisted trilayer graphene. (A, B) Illustrations of two twisted trilayer graphene polytypes, with moiré wavelength λ. The black parallelogram outlines the moiré unit cell in each case. (C, D) Computed local DOS (see Materials and Methods) for 1.2° M-t-B (C) and 1.5° A-t-A (D).

Results and Discussion

Sample Preparation and Characterization: Scanning electrochemical cell microscopy (SECCM) measurements were performed on both nontwisted (ABA, ABC) and twisted trilayer graphene samples, which were fabricated into devices (see Materials and Methods). Fig. 2A shows that naturally occurring ABA and ABC trilayers were mechanically exfoliated from bulk graphite and identified using optical microscopy and confocal Raman spectroscopy (see Materials and Methods and Supporting Information). The M-t-B and A-t-A TTG samples were prepared using the "cut-and-stack" method (see Materials and Methods), resulting in uniform twist angles (θ_m) of approximately 1.34° for the M-t-B device and 1.53° for the A-t-A device. The twist angle distribution and uniformity across the moiré samples were evaluated using piezoelectric force microscopy (PFM) (Fig. 2B) and scanning tunneling microscopy (STM) (Supp. Fig. 5, 10). The AFM images before and after SECCM experiments shows the trilayer graphene and hBN, with residues from the measurements clearly identified (Supp. Fig. 14).

Electrochemical Analysis: Cyclic voltammograms (CVs) measured with $Ru(NH_3)_6^{3+}$ showed that ABA domains exhibited sluggish electro-reduction rates, while ABC domains had more facile kinetics. Both TTG samples displayed highly reversible CVs with significantly higher rate constants compared to ABA and ABC graphene (Fig. 2C). Finite element simulations modeled the quantum capacitance (C_q) and double-layer potential (V_{dl}/V_{app}) for various trilayer systems, revealing that flat electronic bands in TTG led to a more significant partitioning of the applied potential into V_{dl} near the charge neutrality potential (Fig. 3A, 3B). The θ_m dependence of the ET rate constant (k^0) showed a strong, nonmonotonic variation with k^0 ranging over two orders of magnitude (Fig. 3C) .

Unexpected Trends and Structural Analysis: Despite higher DOS and C_q, A-t-A TTG exhibited lower k^0 than M-t-B. B-t-M heterostructures also showed markedly lower k^0 values than M-t-B, indicating that factors beyond ensemble DOS influence interfacial ET kinetics. STM analysis showed significant differences in the area distribution of stacking domains due to lattice relaxation, explaining the kinetic modulation observed at $\theta_m < 2°$ (Fig. 4G). Local DOS profiles showed that enhancements at AAB sites were localized on the top two layers of M-t-B, while DOS at AAA sites were localized on the middle layer of A-t-A. These differences in electronic localization correlated with the observed ET rate constants (Figs. 3C, 5A) .

Implications and Future Work: Theoretical models based solely on θ_m-dependent DOS underestimated the experimental k0 values, suggesting the importance of interfacial electronic coupling, electric double-layer effects, and reorganization energy in ET kinetics. These findings highlight the significant role of electronic localization in interfacial ET and motivate further theoretical work to bridge the gap between theory and experiment, enhancing our understanding of ET processes in twisted trilayer graphene (Figs. 5C-E) .

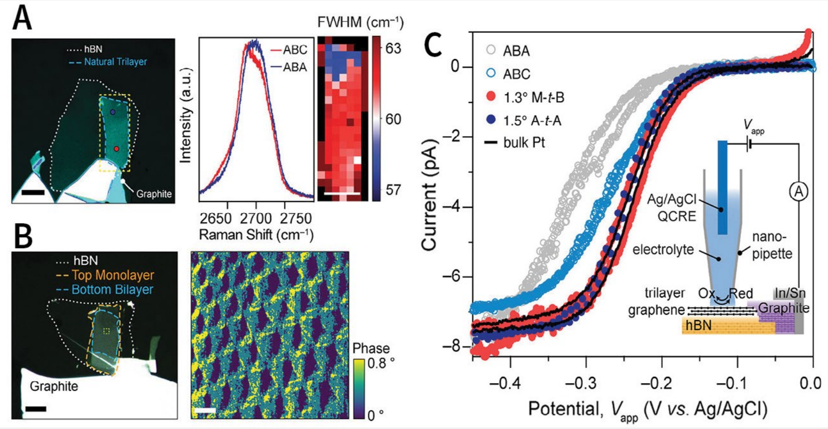

Fig. 2. Fabrication and electrochemistry of twisted trilayer graphene. (A) Left: Optical micrograph of a device fabricated from an exfoliated trilayer graphene flake on hBN. Right: Confocal Raman spectra acquired in the sites in A marked with red (ABC domain) and blue (ABA domain) dots, along with the Raman map of the region indicated with a yellow box in A. Scale bars: 10 μm. (B) Left: Optical micrograph of an M-t-B device on hBN (Scale bar: 10 μm). Right: A lateral PFM phase image over the yellow boxed region in B reveals the moiré superlattice pattern. Scale bar: 50 nm. (C) Representative steady-state voltammograms of 2 mM $Ru(NH_3)_6^{3+}$ in 0.1 M KCl solution obtained at ABA and ABC trilayer graphene, along with 1.3° M-t-B and 1.5° A-t-A, compared to that obtained at an ~40-nm-thick platinum film. Scan rate, 100 mV s^{-1}. The inset illustrates the SECCM technique.

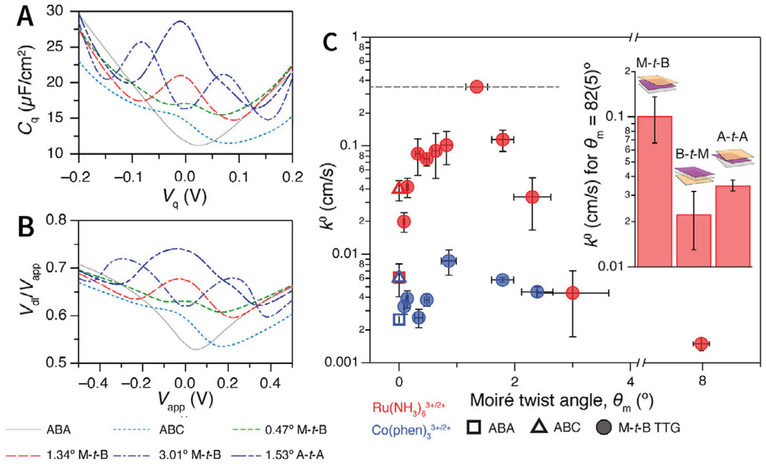

Fig. 3. Angle-dependent quantum capacitance and interfacial ET. (A) Calculated C_q as a function of the chemical potential (V_q) for ABA, ABC, and TTG using the respective computed band structures and DOS profiles (see Materials and Methods). (B) Calculated fraction of applied potential on the double layer (V_{dl}/V_{app}) as a function of the applied potential (V_{app}) for ABA, ABC, and TTG. V_q and Vapp are relative to the charge neutrality potential. Taken together, these data reveal that flat electronic bands result in a more significant fraction of Vapp partitioning into V_{dl} near the charge neutrality potential. (C) Dependence of the ET rate constant, k^0, on the trilayer graphene stacking type (ABA, ABC) and θ_m for M-t-B TTG. Each marker denotes the mean of measurements made on samples within a standard deviation of the mean twist angle. The horizontal and vertical error bars represent the standard deviations of θ_m and the standard error of k^0. The inset shows comparison of k^0 values for M-t-B, B-t-M, and A-t-A TTG at $\theta_m = 0.82 \pm 0.05°$.

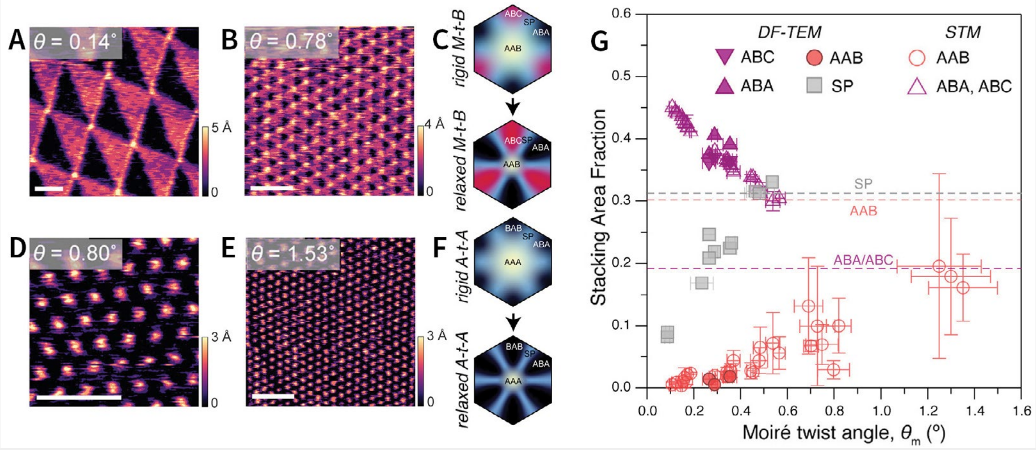

Fig. 4. Lattice relaxation and stacking area fractions in TTG. (A, B, D, E) Constant-current STM images representative M-t-B (A, B) and A-t-A (D, E) samples. Scale bars: 50 nm. (C, D) Qualitative illustrations of different stacking domains in rigid and relaxed M-t-B (C) and A-t-A (F) moiré unit cells. (G) Extracted area fraction of different stacking domains in M-t-B TTG. The horizontal and vertical error bars represent the standard deviations of θ_m and the standard error of the area fraction, respectively.

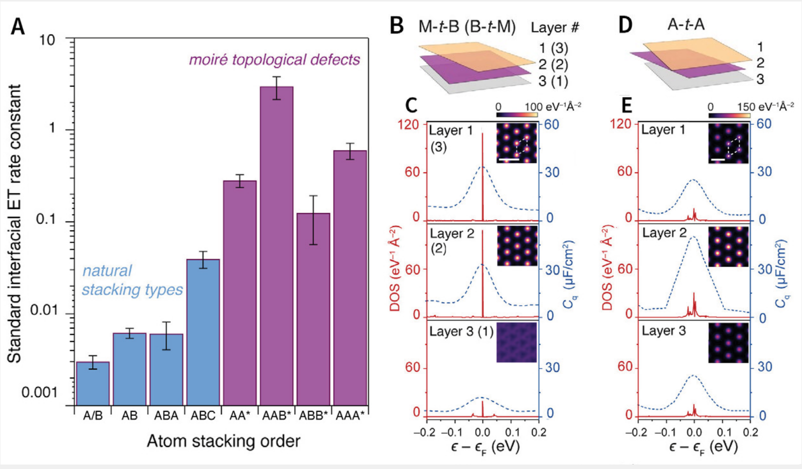

Fig. 5. ET rates of few-layer graphene and layer-dependent DOS localization. (A) Local standard $Ru(NH_3)_6^{3+/2+}$ ET rate constants at few-layer grapheneindifferentstackingconfigurations.“Artificial”moire-́derivedstackingdomainsarelabeled withanasterisk.Eachbaristhemeanlocalrate either measured (for natural stacking) or calculated (for aritifical stacking) for small twist angle samples. The error bars represent the standard errors for the rates. (B) Schematic of M-t-B/B-t-M graphene layers. (C) Layer-dependent DOS profile (see Materials and Methods and Supporting Information Text) for AAB stacking domains in M-t-B and B-t-M graphene at θ_m = 1.2°. Insets show real space DOS maps of each layer at ε = −3 meV. (D) Schematic of the A-t-A layers. (E) Layer-dependent DOS profile for AAA stacking domains in A-t-A graphene at θm = 1.2°. The insets show real space DOS maps of each layer at ε = −1 meV for θ_m = 1.2°.

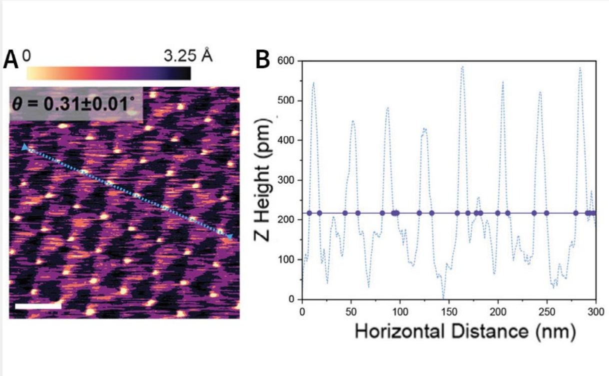

Supp. Fig. 5: STM area fraction analysis. (A) A representative STM image used for area fraction analysis of different stacking domains. The blue dash line was a line scan used for extracting AAB domain width. (B) Line scan Z height over a horizontal distance. The purple line represents the full-width-half-max cutoff used for estimating the AAB radius.

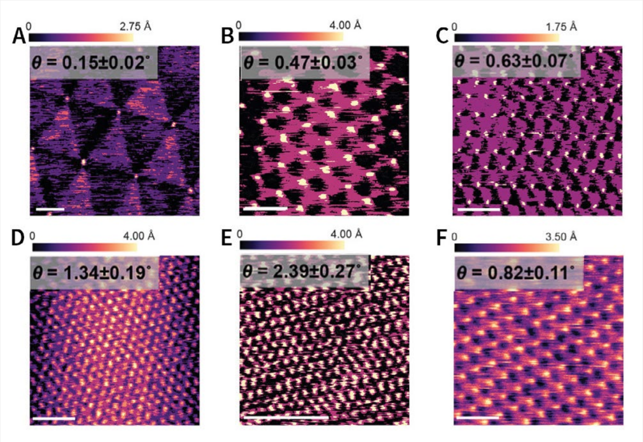

Supp. Fig. 10: Representative STM images of twisted trilayer samples. Representative constant current STM images of various M-t-B in (A) - (E) and B-t-M in (F) of different twist angles.

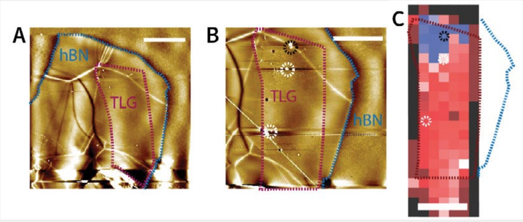

Supp. Fig. 14: Atomic force microscope (AFM) images of a natural trilayer graphene stack. AFM images measured on the same sample before in (A) and after (B) SECCM experiments. The red trace shows the trilayer graphene and the blue trace shows the bottom hBN. Black and white dotted circles highlighted residues from the measurements. Both images were taken on a Park AFM NX10 system with non-contact mode with a set point of 10 nm. (C) Raman map overlayed with the traces of the trilayer graphene and hBN. The measurements on the black dotted circle were used as rates on ABA graphene and those on the white circles were used as rates on ABC. Scale bar: 10 μm.

CONCLUSIONS

Controlling stacking geometries and twist angles in few-layer graphene allows manipulation of standard ET rate constants over three orders of magnitude. Energetically unfavorable topological defects (AAA and AAB stacking domains), achievable only through the construction of a moiré superlattice, exhibit extraordinarily high standard rate constants due to moiré-derived flat bands localized in these defects. In addition to in-plane structural relaxation and electronic localization, the out-of-plane localization of the electron wave function on specific layers of twisted trilayer graphene results in measurable differences in ET rates at topological defects with different symmetries.

These findings demonstrate the sensitivity of interfacial ET kinetics to the three-dimensional localization of electronic states at electrochemical surfaces. They suggest that traditional measurements of ET rates at macroscopic electrodes might underestimate the true local rate constant, mediated by atomic defects that strongly localize electronic DOS at these interfaces. SECCM measurements prove to be powerful tools for probing layer-dependent electronic localization in atomic heterostructure electrodes.

Future experimental and theoretical work is needed to explore the microscopic origins of these electron-transfer modulations, considering reorganization energy, electronic coupling, and the electric double-layer structure. This work highlights the potential of moiré materials as a versatile and systematically tunable experimental platform for theoretical adaptations of the MHC framework, applied to interfaces with localized electronic states, representative of defective surfaces common in real electrochemical systems. In an applied context, twistronics is shown to be a powerful approach for engineering pristine 2D material surfaces to facilitate charge-transfer processes with high kinetics, with implications for electrocatalysis and other energy conversion devices that could benefit from ultrathin, flexible, and/or transparent electrodes with high electron-transfer kinetics.

MATERIALS AND METHODS

Sample Fabrication:

Graphite and hBN were exfoliated using Scotch tape. Monolayer, bilayer, and trilayer graphene were identified using optical contrasts and confirmed by Raman spectroscopy. Trilayer graphene and TTG samples were fabricated using the "cut and stack" dry transfer method on a temperature-controlled heating stage with an optical microscope and micromanipulator. Graphene flakes with both bilayer and monolayer parts were selected for monolayer twist bilayer or bilayer twist monolayer samples. For a-twist-a samples, a large piece of graphene was cut into three pieces and transferred using poly(bisphenol A carbonate) film on PDMS.

Raman Mapping:

Confocal Raman spectra were recorded with a 532 nm laser at 3.2 mW, generating maps with a 2 µm step size. Spectra were fitted with single Lorentzian functions to differentiate ABA and ABC trilayers.

PFM Measurements:

PFM was performed on an AIST-NT OmegaScope with Ti/Ir-coated silicon probes. A 2 V AC bias at 820 kHz and a 25 nN force were used.

STM and AFM Measurements:

STM measurements were conducted using a Park NX10 STM module (Park Systems) at room temperature and atmospheric pressure. AFM measurements were taken by Park AFM NX10 (Park Systems) with non-contact mode with a set point of 10 nm. Pt−Ir tips were prepared by electrochemically etching 0.25 mm Pt−Ir wires (Nanosurf) in 1.5 M $CaCl_2$ solutions. Scanned images were taken with a 0.2 V tip-sample bias and a 100 pA current set point. Twist angles of various samples were determined using Delaunay triangulation on the Gaussian centers.

Electron Microscopy Measurements:

TEM images of nanopipettes were obtained with a JEOL 1200EX microscope at 100 keV. Selected-area electron diffraction patterns were collected on an FEI Tecnai T20 S-TWIN microscope at 200 kV to resolve twist angles. Dark-field images were taken at the National Center for Electron Microscopy.

SECCM Measurements:

SECCM nanopipettes were made from single-channel quartz capillaries (0.7 mm inner, 1.0 mm outer diameter) using a laser nanopipet puller, producing 200 nm diameter pipettes confirmed by TEM. The surfaces were silanized, filled with $Ru(NH_3)_6^{3+}$ or $Co(phen)_3^{3+}$ solutions, and an Ag/AgCl wire was used as a quasi-counter reference electrode. Pipettes approached the target at 0.2 µm/s with a −0.5 V bias (0.5 V for $Co(phen)_3^{3+}$), making contact at >2 pA or <-2 pA. After stabilizing for 30 s, cyclic voltammograms (CVs) were recorded by sweeping the potential at 100 mV/s for five cycles. For small twist samples ($\theta \leq 0.15°$) with moiré wavelengths >80 nm, only CVs from pipettes >200 nm were included. The pipette was retracted by 1 µm and moved horizontally for new measurements.

Chemicals, Finite Element Simulation and CV Fitting, Calculation of Band Structure and DOS:

Please refer to the original paper found at https://doi.org/10.1021/acscentsci.3c00326.

Supporting Information

The Supporting Information is available at https://pubs.acs.org/doi/10.1021/acscentsci.3c00326.

Park FX40

The Ultimate User-Friendly Environmental Solution

Materials sensitive to environmental conditions require meticulous handling during AFM measurements to prevent property changes from exposure to oxygen and humidity. The Park FX40 Environmental Solution addresses this issue by maintaining environmental levels below 1 ppm, offering significant advantages. This integration ensures reliable and accurate measurements easily and efficiently.

▪ Ultra-Low Environmental Contamination

Maintains oxygen and humidity below 1 ppm, perfect for studying materials like Li-ion batteries and perovskites, safeguarding against oxidation and degradation.

▪ Effortless Probe Handling

Includes a Probe Exchanger system for fast, easy probe swaps without inserting hands into the glovebox, thereby minimizing contamination and saving time.

▪ Multi-Sample Versatility

Includes a Multi Sample Chuck and StepScan™ technology that allows for the sequential measurement of multiple samples and different regions, significantly boosting productivity and flexibility in experiments.

▪ One-Click SLD Beam Alignment

Simplifies the setup process, enabling precise alignment easily and rapidly.

Park SYSTEMS

ISOLATION OF PSEUDOCAPACITIVE SURFACE PROCESSES AT MONOLAYER MXENE FLAKES REVEALS DELOCALIZED CHARGING MECHANISM

Marc Brunet Cabré, Dahnan Spurling, Pietro Martinuz, Mariangela Longhi, Christian Schröder, Hugo Nolan, Valeria Nicolosi, Paula E. Colavita & Kim McKelvey. Nature Communications volume 14, Article number: 374 (2023)

ABSTRACT

Pseudocapacitive charge storage in $Ti_3C_2T_x$ MXenes in acid electrolytes is typically described as involving proton intercalation/deintercalation accompanied by redox switching of the Ti centres and protonation/deprotonation of oxygen functional groups. Here we conduct nanoscale electrochemical measurements in a unique experimental configuration, restricting the electrochemical contact area to a small subregion (0.3 µm²) of a monolayer $Ti_3C_2T_x$ flake. In this unique configuration, proton intercalation into interlayer spaces is, and surface processes are isolated from the bulk processes, characteristic of macroscale electrodes. Analysis of the pseudocapacitive response of differently sized MXene flakes indicates that entire MXene flakes are charged through electrochemical contact of only a small basal plane subregion, corresponding to as little as 3% of the flake surface area. Our observation of pseudocapacitive charging outside the electrochemical contact area is suggestive of a fast transport of protons mechanism across the MXene surface.

Introduction

A low-carbon economy based on renewable energy needs energy storage technologies. Supercapacitors bridge the gap between rechargeable batteries and traditional capacitors, with both high-power and high-energy density. Developing new supercapacitor technology depends on understanding the electrochemical charge storage mechanism and developing new materials.

MXenes, two-dimensional materials from transition metal carbides, nitrides, and carbon-nitrides, are excellent supercapacitors due to their high surface area, conductivity, and pseudocapacitive response. Titanium carbide MXenes ($Ti_3C_2T_x$) have specific gravimetric capacitances of about 250 F/g and store charge through ion intercalation and change in oxidation state. On macroscale electrodes, surface processes occur at shorter timescales, while bulk processes occur at longer timescales, affecting ion transport throughout the material network.

The study quantifies the intrinsic electrochemical pseudocapacitive response of monolayer $Ti_3C_2T_x$ MXene using scanning electrochemical cell microscopy (SECCM) to isolate capacitive response on 0.3 µm² regions. The SECCM configuration eliminates bulk effects and allows measurement of surface-dependent processes contributing to the pseudocapacitive response. Cyclic voltammograms are obtained on a grid of sample points spaced 1.80 µm apart on $Ti_3C_2T_x$ flakes and surrounding carbon substrate for comparison.

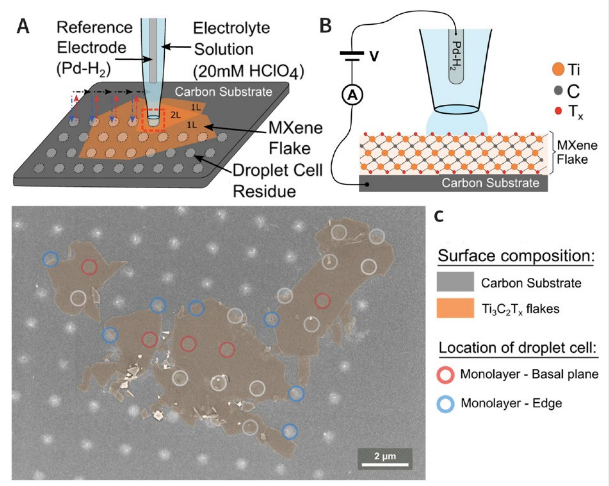

Fig. 1. (A) Schematic of the SECCM configuration for measuring monolayer $Ti_3C_2T_x$ flakes immobilized on a carbon supporting electrode surface. SECCM-based cyclic voltammogram measurements were conducted in a hopping mode, with the probe movement pattern shown in coloured arrows (blue approach, red retract, black move to next measurement position). (B) Schematic of end of SECCM probe, highlighting the nanoscale electrochemical droplet cell at the end of the SECCM probe and the two-electrode electrochemical cell configuration. (C) Electron micrograph of sample surface containing monolayer MXene immobilized on a carbon surface after SECCM measurements, with each SECCM sample location highlighted according to the surface composition.

Results

$Ti_3C_2T_x$ flake characterization

Characterization of $Ti_3C_2T_x$ flakes was conducted by liquid exfoliation of MAX phase ($Ti_3C_2T_x$) to obtain a stock dispersion. Freestanding films were prepared via vacuum filtration using the stock $Ti_3C_2T_x$ dispersions (28 mg/ml). X-ray diffraction (XRD), energy-dispersive X-ray spectroscopy (EDX), and Raman spectroscopy were performed to confirm the presence of $Ti_3C_2T_x$. Atomic force microscopy (AFM) and scanning electron microscopy (SEM) were used to determine the morphology of the flakes, which were found to be monolayer.

Localized electrochemical measurements on $Ti_3C_2T_x$ flakes

Localized electrochemical measurements on $Ti_3C_2T_x$ flakes were conducted using a scanning electrochemical cell microscopy (SECCM) approach. Backscattered SEM images showed the electrolyte residues remaining after SECCM measurements, with a total of 80 points identified. Of these, 64 points had a well-defined circular geometry, allowing for the determination of the electrochemical surface area (0.31 ± 0.03 µm^2). 24 points (Fig. 1C) were found to partially or completely contact the MXene flake, with 5 located on the basal plane of the monolayer $Ti_3C_2T_x$. 40 points were identified as contacting the carbon substrate exclusively.

Representative voltammograms on the carbon surface and on the basal plane of monolayer $Ti_3C_2T_x$ flakes (Fig. 2A) were obtained. Between +0.5 and -0.5 V vs Pd-H_2 (Pd-H_2 is +50 mV vs SHE), the voltammograms obtained over $Ti_3C_2T_x$ flakes (Fig. 2) showed the characteristic i-V curves of pseudocapacitive charging in acidic media. Below -0.6 V vs Pd-H₂, an exponential increase in the current magnitude was observed vs applied potential on both $Ti_3C_2T_x$ flakes and the carbon substrate, which is consistent with the onset of the hydrogen evolution reaction (HER).

The potential window of -1 to 0.5 V vs Pd-H_2 was chosen to induce pseudo-capacitive and HER responses without inducing irreversible anodic oxidation, which occurs above +0.7 V vs Pd-H_2 (+0.75 V vs SHE). The first cycle over each point of the SECCM was used as a conditioning step10, and the capacitance response was determined from the second cycle. The SECCM configuration prevents MXene flakes from lifting off from the surface due to mechanical instability issues that are common of macroscale MXene electrodes when placed under electrolyte19. Additionally, the SECCM droplet cell ensures rapid gas transport to the liquid-air interface to prevent bubble formation during hydrogen evolution. AFM and SEM images show that the MXene layers are intact on the carbon working electrode support and show no evidence of exfoliation.

Observation of capacitive responses on subregions of $Ti_3C_2T_x$ flakes

The capacitance was determined by integrating charge between +0.5 and −0.5 V vs Pd–H_2 (Fig. 2A). A histogram of the capacitance values (N=80) is displayed in Fig. 2B, and the capacitance was normalized by the geometric area to derive the specific surface capacitance at each point (Fig. 2C). The average surface capacitance obtained for carbon was 0.15±0.04 mF/ cm^2, and the average surface capacitance measured on monolayer $Ti_3C_2T_x$ MXene sample points was 2.8±1.0 mF/ cm^2, more than an order of magnitude larger than that of the carbon support. The broad distribution in specific surface capacitance is due to a wide range of flake morphologies (e.g., edge, multilayer).

MXene capacitive values are often compared using gravimetric capacitance metrics. Experiments using macroscopic electrodes normalize capacitance by the mass of electrode material deposited over the contacted area. Computational work translates monolayer simulations of specific areal capacitance into gravimetric capacitances. In our SECCM experiments, we measure the electrochemical contacted area (0.31 µm^2) and calculate the equivalent mass of MXene contacted (1.15±0.10 fg). This yields gravimetric capacitances between 4000 and 12,000 F/g for a monolayer basal plane, one to two orders of magnitude greater than any previous theoretical prediction or measurement. The $Ti_3C_2T_x$ pseudocapacitive charging is estimated to provide 0.4 e- per unit cell per volt of storage when both sides of a monolayer are protonated. A gravimetric capacitance of 12,000 F/g would be equivalent to 14.8 e- per unit

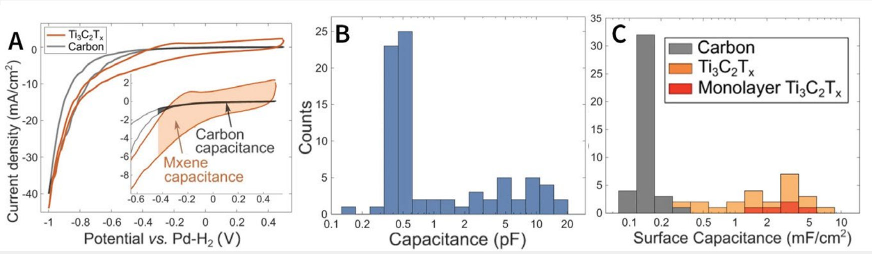

Fig. 2. Capacitive response on monolayer MXene flakes and surrounding carbon substrate. a Representative cyclic voltammograms over a carbon surface (black) and a single monolayer MXene flake (orange) at scan rate of 0.5 V/s in 20 mM $HClO_4$. b Histogram of the capacitance at each individual SECCM grid point observed on the SEM image (N=80). c Stacked histogram of the surface capacitance over carbon surface (black, N=40) and MXene flake (orange, N=24), of which the basal plane of single layer $Ti_3C_2T_x$ points are highlighted (red, N=5).

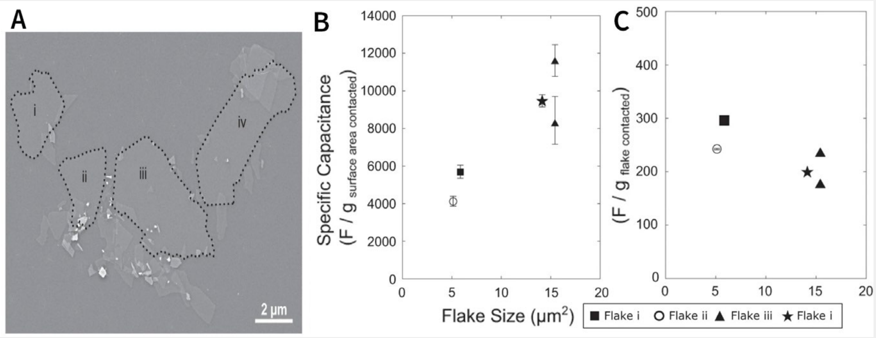

Fig. 3. Monolayer MXene capacitive response dependence on flake size. (A) Electron micrograph of sample surface with flakes larger than 5 µm^2 labelled. (B) Specific gravimetric capacitance on monolayer $Ti_3C_2T_x$ compared to the total area $Ti_3C_2T_x$ flake, obtained by normalizing capacitance by the mass of MXene in electrochemical contact with electrolyte. (C) Specific gravimetric capacitance obtained by normalizing by the total mass of the monolayer flake. Error bars represent the standard deviation from determination of (B) MXene mass contacted and (C) MXene flake mass.

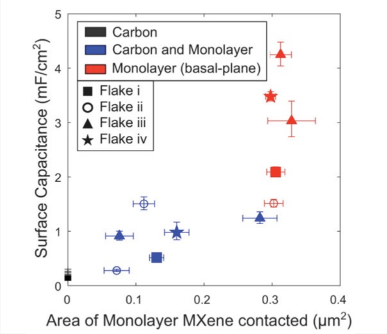

Fig. 4. Capacitance on edge and basal plane of monolayer MXene flakes. Surface capacitance plotted against the area of $Ti_3C_2T_x$ monolayer contacted. Different symbols indicate which flake was contacted, while colour code indicate surface type. Data shows the mean and error bars represent the standard deviation.

cell per volt, suggesting the MXene monolayer area engaged in capacitive charging is much larger than the area of the submicron droplet contact (0.31 μm^2).

SEM imaging reveals four separate monolayer flakes in the MXene sample (Fig. 3A). Fig. 3B shows differences in basal plane pseudocapacitance values (N = 5) between the flakes, with increasing capacitance with increasing flake size. Normalizing the basal-plane capacitance values by the mass of the entire flake yields specific gravimetric capacitance values of 180-300 F/g (Fig. 3C), in agreement with DFT simulations (ca. 230 F/g) and previous experimental determinations (220–250 F/g). Normalizing by the two-sided area of the entire monolayer flake yields specific surface capacitance values of 40 ± 10 μF/cm^2, in agreement with DFT prediction for $Ti_3C_2T_x$ of 45 μF/cm^2, suggesting the capacitance response arises from the entire MXene flake.

Implications for MXene pseudocapacitive mechanism

MXene pseudocapacitance arises from proton intercalation/deintercalation accompanied by redox switching of Ti centres and protonation/deprotonation of oxygen functional groups, yet our samples consist of monolayer MXene on a carbon surface, with electrochemical contact to only a fraction of the basal plane, leaving no clear pathway for ion intercalation. Nonetheless, we measure pseudocapacitance from the entire MXene flake, despite ion transport to only 3% of its surface.

Ion intercalation at flake edges may not be responsible for the pseudocapacitive values shown in Fig. 3, as edge points show a smaller capacitance value per area of MXene contacted than basal-plane monolayer points (Fig. 4). However, contact between the flake edge and the carbon substrate may enable intercalation, potentially providing an enhanced capacitive response.

Discussion

The Dunn et al. model is often used to deconvolute capacitive I–V curves obtained on macroscopic 3D electrodes into current contributions from both surface and bulk processes. However, it only considers two possible charging processes and assumes that the transport of charged species is a one-dimensional linear diffusion process, which is a limitation for the description of 3D hierarchical structures. Other transport mechanisms can be included to improve deconvolution, but this increases the complexity of the modelling and can lead to non-unique solutions.

This study suggests that pseudocapacitive charging outside the wetted area of MXene flakes is likely due to surface diffusion of protons in a water adlayer on the MXene flake surface. The AFM step-height profile of $Ti_3C_2T_x$ flakes suggests the presence of water adsorbed on its surface and/or water trapped between the carbon substrate and the $Ti_3C_2T_x$ flake. Proton mobility/diffusivity at hydrophilic surfaces is high, with diffusion coefficients >10−8 cm^{2}s^{-1}, which is enough to access a 10 μm^2 flake surface during the electrochemical measurements.

MXene-based supercapacitors have been found to have very high specific gravimetric capacitances, even with limited percolation contacts. This is due to proton transport across the MXene surface at diffusion coefficients >10−8 cm^2 s^{-1}, which acts as a complementary mechanism to proton intercalation/deintercalation into MXene interlayer spaces. This allows for ultrafast charging/discharging rates (>1000 V/s).

Methods

Chemicals

Perchloric Acid ($HClO_4$, Fluka Analytical, 67–72%) and Millipore water (18 MΩ cm) were used as supplied at room temperature.

Preparation of carbon substrates, $Ti_3C_2T_x$ stock solution, and monolayer MXene flakes supported on carbon electrodes

Carbon substrates were synthesized on SiO_2/Si wafers via sputtering deposition followed by graphitization under inert atmosphere (300 nm thermal oxide, cleaned with piranha solution, rinsed with Millipore water, dried under nitrogen, sputter-deposited with graphite target at a base pressure <2 × 10−6 mbar for 40 min using Ar as deposition gas (50 sccm, 1–2 × 10−2 mbar), graphitized at 900 °C in a tube furnace under N2 flow for 60 min).

$Ti_3C_2T_x$ stock solution was prepared by adding 20 ml of 9 M HCl (Sigma) to a PTFE vented vessel containing 1.6 g of LiF powder (Sigma), stirring at 400 rpm for 10 min while the vessel was placed in a 35 °C oil bath, adding 1 g of MAX $Ti_3C_2T_x$ phase (Carbon-Ukraine ltd.), keeping the solution at 35 °C and stirring at 400 rpm for 24 h, diluting with deionized water and centrifuging for 5 min at 2800 × g (5000 rpm), redispersing sediment in deionized water and centrifuging again for 5 min at 2800 × g (5000 rpm) until pH 6, vortexing for 30 min to ensure delamination of multilayer $Ti_3C_2T_x$ flakes into monolayer $Ti_3C_2T_x$ flakes, centrifuging for 30 min at 250 × g (1500 rpm) and collecting supernatant containing monolayer flakes, and centrifuging for 1 hour at 2800 × g (5000 rpm) to concentrate monolayer flakes in sediment.

Monolayer MXene flakes were supported on carbon electrodes by diluting $Ti_3C_2T_x$ stock solution with distilled water down to 10 μg/ml, bubbling with argon to degas, filling flask with argon, drop-casting 2 μl of diluted solution onto carbon substrates, and leaving to dry overnight in air. Electrochemical measurements were carried out within 1 day.

Instruments

Optical, AFM, and SECCM measurements of monolayer MXene flakes supported on carbon electrodes were acquired on a Park NX10 (Park Systems, South Korea). AFM and SECCM measurements were done in a room with temperature control (22.6 ± 0.2 °C, 40-60%RH). SEM and EDX were performed on a Zeiss Ultra Plus field-emission SEM (3 kV, 10 keV). XRD was obtained using a Bruker D8 Discovery (3-75°, 2° min−1). Raman spectroscopy was acquired using a WITec Alpha 300R (633 nm He-Ne laser, 1800 lines/mm grating). Structural characterization measurements (EDX, Raman, XRD) were performed on as-synthesized $Ti_3C_2T_x$ thin film produced by vacuum filtration.

Probe preparation

SECCM probes were single-barrelled nanopipettes (1.5 mm O.D and 0.86 mm I.D., BF150-86-7.5, Sutter Instrument, USA) with ~400 nm aperture radius, filled with 20 mM $HClO_4$ electrolyte and a Pd-H_2 QRCE (0.25 mm diameter, 5 cm long, PD005130, Goodfellow, UK) biased at −3 V vs. a Pt counter electrode in 20 mM $HClO_4$ solution for 15 min. After the SECCM scan, the Pd–H_2 QRCE was calibrated against the SCE with a value of −191 mV, corresponding to +50 mV vs SHE.

Scanning protocol

Electrochemical SECCM measurements were performed over a sample region with monolayer $Ti_3C_2T_x$ flakes (see Supp.

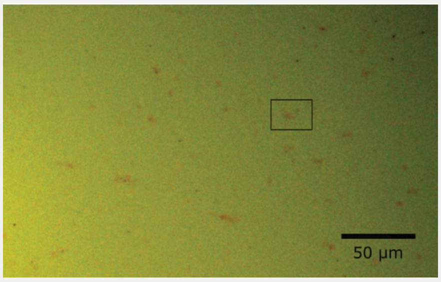

Supp. Fig. 4. Optical image of substrate with $Ti_3C_2T_x$ drop-cast. Black square indicates the region of sample where experiments were conducted.

Fig. 4). SECCM imaging was done on a 1.8 µm grid. At each point two cyclic voltammograms were measured between +0.5 and −1 V vs. Pd–H_2 (scan rate 0.5 V/s) over both flakes and substrate. A hopping mode was used with a vertical approach speed of 0.2 µm/s and a potential of −0.5 V until contact (detected by a double layer charging current >3.0 pA). After contact, the potential was changed to +0.5 V and two voltammetry cycles were recorded; then the pipette was retracted and moved to the next sample point. SECCM scans with $HClO_4$ left smaller droplet residues than H_2SO_4, enabling AFM scanning to resolve monolayer and bilayer MXene flake steps.

References and Supplemental Information

News you might have missed...

INTRODUCING PARK FX200, THE MOST ADVANCED AFM FOR 200 MM SAMPLES FROM PARK SYSTEMS

July 2024

Park Systems, a leading manufacturer of nano-metrology systems, announced the release of its latest atomic force microscopy (AFM) innovation, Park FX200, designed for 200 mm samples. The FX200 is developed to meet the needs of both research and industrial applications, offering significant advancements in large-sample AFM technology.

The FX200 features an advanced mechanical structure that ensures a significantly lower noise floor and minimal thermal drift, providing increased stability during measurements. This enhancement promotes greater accuracy and reliable performance over extended operation periods.

With faster Z servo performance, the FX200 enables rapid and precise scanning across large sample areas. Its enhanced high-power sample view with autofocus allows researchers to achieve exceptional clarity and detail in AFM imaging, regardless of sample type or condition.

The FX200 includes several automated features to streamline operations and maximize efficiency. Automatic probe recognition and exchange eliminate manual adjustments, while a reduced laser spot size and automatic alignments improve measurement accuracy and consistency.

Macro optics provides a full 200 mm sample view, allowing comprehensive analysis without the need for stitching multiple images. This capability is enhanced by automatic sequential measurements at predefined coordinates, facilitating efficient data collection across large sample areas.

Park FX200 is designed with user convenience in mind, featuring automatic AFM scan parameter settings. This intuitive interface allows researchers to focus on their scientific objectives rather than instrument configuration, enhancing productivity and workflow efficiency.

Furthermore, its superior performance capabilities make it ideal for a wide range of research and industrial applications, including investigating surface morphology, characterizing mechanical properties, and exploring nanoscale phenomena, delivering reliable results for contemporary scientific endeavors. Representing a significant advancement in AFM technology, Park FX200 offers enhanced precision, automated efficiency, and comprehensive sample visualization.

SUCCESSFUL NANOSCIENTIFIC SYMPOSIUM SE ASIA 2024 AND EXCITING GLOBAL LINEUP FOR 2024 NANOSCIENTIFIC SYMPOSIUMS

Park Systems announced the successful conclusion of the NANOscientific Symposium SE Asia 2024. The event was held at Chulalongkorn University in Bangkok, Thailand, on August 6-7. It brought together leading experts, researchers, and scientists from around the globe. This year's symposium was a vibrant hub for discussing the latest advancements in nanoscience and nanotechnology, further solidifying its reputation as a premier platform for innovation and collaboration in the field.

Highlights from the NANOscientific Symposium SE Asia 2024

The symposium featured distinguished speakers, including experts from Chulalongkorn University, Nanyang Technological University, TMEC-NECTEC, IISER TVM, and Park Systems Corp. Discussions covered a range of topics, with a focus on scanning probe microscopy (SPM) and imaging spectroscopic ellipsometry (ISE) in various applications.

Speeches highlighted advancements such as an optical fiber sensor for detecting diabetes biomarkers and nanomechanical mapping of viral proteins. Cutting-edge AFM techniques like scanning microwave impedance microscopy and 3D-AFM were showcased for nanoscale imaging. Other topics included improvements in piezoelectric nanogenerators, scalable perovskite solar cell processes, and light-responsive nanoparticles for drug delivery.

A poster session featured innovative research from Asia, with Kankan Swargiary from Chulalongkorn University winning the best poster award for a cost-effective method of growing ZnO nanostructures on optical fibers. Participants also experienced live demonstrations of Park's advanced AFM technologies at the Nano-Engineering Innovative Design Center, gaining hands-on insights into nanotechnology applications. The event fostered collaboration and networking among academics, industry professionals, and researchers, with attendees praising its impact on their work.

Looking Ahead: The 2024 NANOscientific Symposiums

Building on the success of the NSS SE Asia symposium, Park Systems announced the upcoming schedule for the 2024 NANOscientific Symposiums, set to take place in major global regions. These events, known for uniting thousands of international attendees and promoting rich discussions and collaborations in nanoscience, will be held as follows:

- **Japan:** Tokyo Institute of Technology – October 18
- **China:** SINANO, Chinese Academy of Sciences, Suzhou – October 26-27
- **Europe:** Fraunhofer EMFT, Munich, Germany – October 29-31
- **Americas:** Arizona State University, Phoenix, Arizona – November 13-14
- **Korea:** Paradise Hotel, Busan – November 21

Each symposium will cover a broad spectrum of topics, including electrical properties in semiconductors, 2D materials, surface science, and molecular biology, with a special emphasis on the practical applications of nanoscience in both industry and academia. Researchers worldwide are encouraged to submit their papers and posters for consideration, with prizes awarded for outstanding presentations.

For more information on the regional symposiums, including registration details, please visit NANOscientific.org/nss2024. Updates on symposium topics, keynote speakers, and other event details will be progressively announced on the website

About NANOscientific Symposiums

The NANOscientific Symposiums are a series of events sponsored by Park Systems that bring together the global nanoscience community to share research, foster collaboration, and explore the latest innovations in nanotechnology. Since their inception, these symposiums have grown into a key platform for advancing the field of nanoscience, connecting researchers, and inspiring the next generation of scientific breakthroughs.

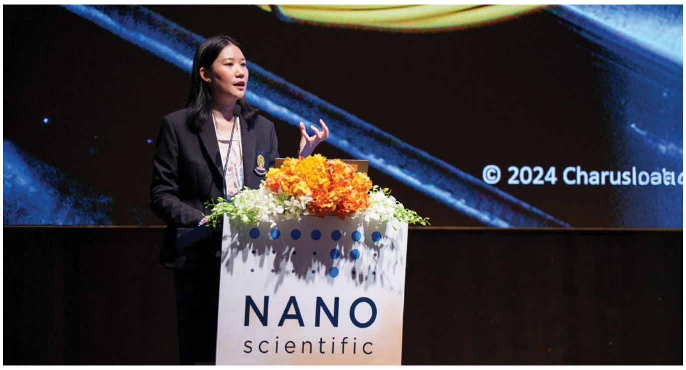


NANO
scientific

NANOscientific Symposium 2024

REGISTER NOW!

nanoscientific.org/nss2024

The 2024 NANOscientific Symposium is set to be a landmark event, uniting global experts in the fields of nanoscience and nanotechnology. This year, we extend our focus beyond Scanning Probe Microscopy (SPM) to encompass a broader range of nanotechnological applications and innovations. With an enriched agenda featuring keynote presentations from trailblazers in the industry, interactive sessions, and enhanced virtual networking opportunities, attendees will have unprecedented access to resources and collaborations that drive research, innovation, and commercial success in the ever-evolving world of nanotechnology.


NSS Americas
13 - 14 Nov | Phoenix, USA


NSS Korea
21 Nov | Busan, Korea


NSS SE Asia
06 Aug | Bangkok, Thailand


NSS Japan
18 Oct | Tokyo, Japan


NSS China
26 - 27 Oct | Suzhou, China


NSF Europe
29 - 31 Oct | Munich, Germany

Sponsored By

Park SYSTEMS

NANOTECHNOLOGY WORLD